Analysis of a Helix Antenna Using a Moment Method Approach With Curved Basis and Testing Functions

Eric D. Caswell

Thesis submitted to the Faculty of the
Virginia Polytechnic Institute and State University
in partial fulfillment of the requirements for the degree of

Masters of Science
in
Electrical Engineering

William A. Davis, Chair
Warren L. Stutzman
Gary S. Brown

September , 1998
Blacksburg, Virginia

Keywords: Helix, Method of Moments, Curved Segments

Analysis of a Helix Antenna Using a Moment Method Approach With Curved Basis and Testing Functions

Eric D. Caswell

(ABSTRACT)

Typically wire antenna structures are modeled by approximating curved structures with straight wire segments. The straight wire approximation yields accurate results, but often requires a large number of segments to adequately approximate the antenna geometry. The large number of straight wire segments or unknowns requires a large amount of memory and time to solve for the currents on the antenna. By using curved segments which exactly describe the contour of the antenna geometry the number of unknowns can be reduced, thus allowing for bigger problems to be solved accurately.

This thesis focuses on the analysis of a helix antenna. The Method of Moments is used to solve for the currents on the antenna, and both the triangle basis and pulse testing functions exactly follow the contour of the helix antenna. The thin wire approximation is used throughout the analysis. The helix is assumed to be oriented along the z-axis with an optional perfect electric conductor (PEC) ground plane in the x-y plane. For simplicity, a delta gap source model is used. Straight feed wires may also be added to the helix, and are modeled similarly to the helix by the Method of Moments with triangular basis and pulse testing functions.

The primary validation of the curved wire approach is through a comparison with MININEC and NEC of the convergence properties of the input impedance of the antenna versus the number of unknowns. The convergence tests show that significantly fewer unknowns are needed to accurately predict the input impedance of the helix, particularly for the normal mode helix. This approach is also useful in the analysis of the axial mode helix where the current changes significantly around one turn. Because of the varying current distribution, the improvement of impedance convergence with curved segments is not as significant for the axial mode helix. However, radiation pattern convergence improvement is found. Multiple feed structures for the axial mode helix are also investigated. In general, the many straight wire segments, and thus unknowns, that are needed to accurately approximate the current around one turn can be greatly reduced by the using the curved segment method.

Acknowledgments

I would like to thank my advisor, Dr. William A. Davis, for all of his advice and motivation throughout the completion of this thesis. His technical knowledge was an invaluable asset, but maybe more importantly, he helped to keep me focused and pointed in the right direction. I would also like to thank my other committee members, Dr. Warren L. Stutzman and Dr. Gary S. Brown, for their suggestions and insight.

Also, I would like to thank my family for their support and encouragement. In particular, my desire to avoid the question “Have you finished your thesis yet?” provided me with great motivation to complete this thesis.

Table of Contents

List of Figures

1. Introduction

1.1 Thesis Motivation

Wire antennas are usually analyzed using codes such as the Numerical Electromagnetics Code (NEC) and MININEC which use straight wires to model all antenna structures. This can be a very inefficient method in terms of unknowns or computer memory for modeling curved wire antennas. For some antennas many small, straight wire segments are required to accurately model the curved geometry of the antenna. Often the number of straight wire segments needed to approximate the geometry of the antenna exceeds the number of unknowns needed to model the current distribution on the antenna. By using curved segments, which can exactly follow the contour of the antenna structure, the problem of modeling the antenna geometry can be greatly reduced. In this thesis, a Method of Moments computer code, called the Curved code, will be developed which uses curved basis and testing functions. A helix antenna will be used to demonstrate the improvements that can be achieved by using the Curved code. Properties of the helix such as current distribution, bandwidth, radiation pattern, and feed effects will also be investigated in conjunction with the testing of the Curved code.

1.2 Literature Review

Helical antenna analysis and the more recent numerical modeling of such antennas with the Method of Moments are well established fields of study. In the late 1940s, J. D. Kraus wrote many papers detailing the properties of helical antennas, which were later included in his book, Antennas, (1950). Others such as Wheeler (1947), Roy (1969), and Marsh (1951) were early contributors to the study of helical antennas. As wireless communications become more wide spread, helix analysis for handheld devices is gaining importance. The effects of finite ground planes (Desplanches, et al, 1997), dielectric loading (Hui, et al , 1997), and dual frequency techniques (Haapala et al, 1996) on helix operation are current areas of interest.

The use of integral equations to study wire antennas and scatterers dates back to Pocklington (1897) and Hallen (1938). In the 1960s many papers were published on the subject. Much of the early numerical work was performed by R. F. Harrington and is contained in his book, Field Computations by Moment Methods (1968). Richmond (1965), Mei (1965), and King (1967) were also key contributors to the field of wire antenna analysis. Work continues to this day in a effort to improve the computational efficiency of the techniques described in the papers mentioned above.

One method of improving the computational efficiency of wire antenna analysis with the Method of Moments is using curved segments. The use of curved segments can be implemented using various techniques with differing degrees of approximation. A paper by Medgyesi-Mitschang and Putnam (1985) models a curved wire following a

circular arc with one curved segment and a sinusoidal current expansion. Their formulation is adapted to wires without a constant radius of curvature by using entire domain expansion functions defined by a parametric representation of the wire locus. Another method is to use quadratic segments to approximate the curve of the antenna (Champagne, et al, 1992). Champagne found that by using quadratic segments to model a loop antenna and Archimedian spiral memory and computation time can be reduced. A generalized superquadratic loop, that is circular, elliptic, and rectangular loops, was modeled using a parametric description of curved segments with piece-wise sinusoidal basis and testing functions (Jensen and Rahmat-Samii, 1994). A similar technique outlined in (Li, et al, 1996) uses a parametric equation to model the wire antenna and quadratic B-spline basis functions of the parameter to approximate the current. This technique was also applied to loop and spiral antennas. It is also possible to improve on the straight wire approximation by creating a new set of basis functions which are a weighted sum of the original basis functions (Rogers and Butler, 1997). The new basis functions span several of the original basis functions reducing matrix rank and computation time. Khamas, et al, (1997a, 1997b) modeled Archimedian and logarithmic printed wire spirals using piece-wise sinusoidal basis and testing functions following the exact curve of the antenna. Again, reduced memory space was obtained for accurate results.

The results obtained from the Curved code will be compared to MININEC Professional for Windows (Rockway and Logan, 1995), NEC (Burke, 1992), and WIRE (Davis, 1995) in this thesis. All three of the codes use a straight wire approximation to model curved, wire antennas, but they don't all use the same current approximation. MININEC and WIRE use triangular basis and pulse testing functions while NEC uses sinusoidal interpolation basis and delta testing functions. Throughout this thesis, MININEC Professional for Windows will be referred to as MININEC Pro or simply MININEC. NEC will refer to NEC-WIN Pro, which is a user interface for the NEC2 or NEC4 computational engine. The NEC2 engine was used in this thesis, however, the results did not differ significantly from those obtained with NEC4. WIRE was written by Dr. W.A. Davis at Virginia Tech and is based on the concepts developed in MININEC. WIRE is available on Dr. Davis' web site.

1.3 Thesis Overview

Chapter 2 of this thesis discusses the background theory of straight wire antenna analysis. The electric field integral equation is derived and the Method of Moments is presented. A resonant half-wave dipole is used to demonstrate impedance and current distribution convergence. The concepts of Chapter 2 for the straight wire antenna are extended in Chapter 3 for arbitrarily shaped wire antennas. The helix antenna is chosen to demonstrate the improvement found when using curved segments. Along with the general form of the electric field integral equation, the helix geometry and parameters, wire connection concepts, and the perfect electric conductor (PEC) ground plane formulation are presented in Chapter 3.

The next two chapters make use of the concepts developed in Chapters 2 and 3 to analyze a helix antenna. First, Chapter 4 looks at the results from NEC, MININEC, and the Curved code for a normal mode helix. The primary characteristic that will be considered is impedance convergence versus the number of segments used to model the antenna. Then, the axial mode helix is investigated in Chapter 5. The convergence properties for both an axial mode helix in free space and over an infinite PEC ground plane are shown. Both impedance and radiation pattern convergence are considered. The effects of different feed structures for the axial mode helix over ground are also presented. Finally, conclusions and recommendations for additional work are discussed in Chapter 6.

2. Background Theory

This chapter presents the theory for the solution of the currents on straight wire antennas using the Method of Moments (Harrington, 1968). The first step in developing the solution for the currents is to derive the appropriate electric field integral equation. The Method of Moments will then be used to convert the integral equation into a system of linear equations which can be solved by various techniques of linear algebra. The electric field integral equation and Method of Moments are general relationships, but are usually applied to straight wire antenna geometry's as presented in this chapter. This theory is the basis of the development for a helix antenna using the actual curved wire contour to be presented in the next chapter.

2.1 Electric Field Integral Equation for Wire Antennas

The first step in developing the solution for the current on a wire antenna is determining the appropriate integral equation. The starting point in deriving the electric field integral equation (EFIE) is Maxwell's equations in the frequency domain,

$$\nabla \times \vec{E} = -j\omega\mu\vec{H} - \vec{M} \tag{2.1}$$

$$\nabla \times \vec{H} = j\omega\varepsilon\vec{E} + \vec{J} \tag{2.2}$$

$$\nabla \cdot \vec{E} = \frac{\rho_e}{\varepsilon} \tag{2.3}$$

$$\nabla \cdot \vec{H} = \frac{\rho_m}{\mu}, \tag{2.4}$$

along with the continuity equations,

$$\nabla \cdot \vec{J} = -j\omega\rho_e \tag{2.5}$$

$$\nabla \cdot \vec{M} = -j\omega\rho_m . \tag{2.6}$$

In the above equations, $\vec{E}$ and $\vec{H}$ are the electric and magnetic field intensities, $\vec{J}$ and $\vec{M}$ are the electric and magnetic current densities, and ρ_e and ρ_m are the electric and magnetic charge densities respectively. The media is assumed to be linear, isotropic, and homogenous so that the permittivity, ε, and permeability, μ, may be removed from the curl and divergence operations. The boundary conditions on the magnetic and electric fields at the surface, S, as shown in Fig. 2.1 are

$$\hat{n} \times (\vec{H}_2 - \vec{H}_1) = \vec{J}_s \tag{2.7}$$

$$\hat{n} \times (\vec{E}_2 - \vec{E}_1) = -\vec{M}_s . \tag{2.8}$$

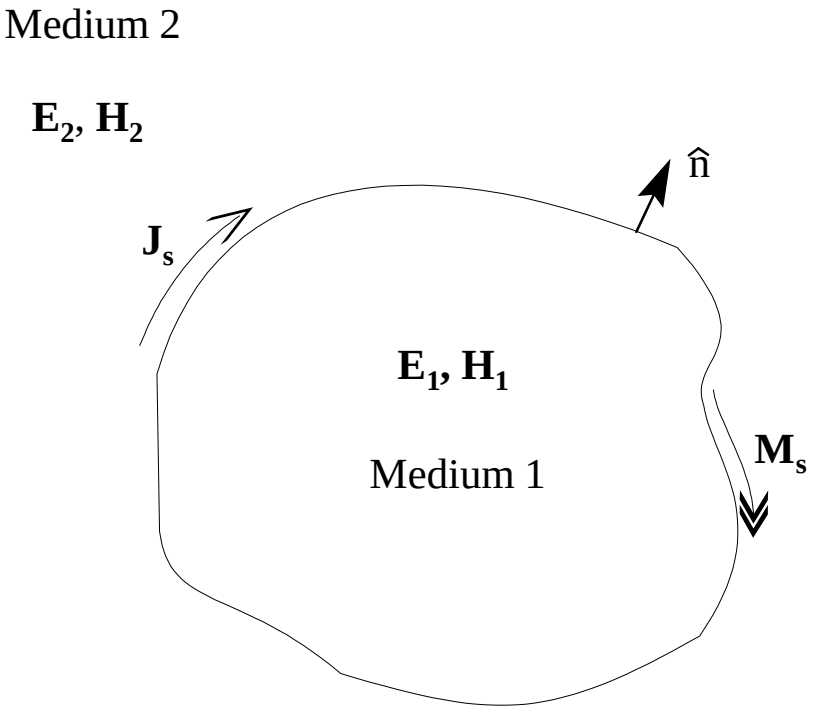

Figure 2.1 Geometry for the general scattering problem.

If medium 1 is a perfect electric conductor (PEC), the fields inside the surface will become zero and the boundary condition on the electric field becomes

$$\hat{n} \times (\vec{E}_2) = 0. \tag{2.9}$$

The electric field outside of S, $\vec{E}_2$, may be written as the sum of an incident electric field, $\vec{E}_i$, and a scattered electric field, $\vec{E}_s$. The incident electric field induces the surface current $\vec{J}_s$ which in turn creates the scattered field $\vec{E}_s$. The Equivalence Principle can be used to remove the PEC giving a homogeneous free space problem. For the PEC case, the equivalent current equals the induced current, $\vec{J}_s$.

Making use of the fact that the divergence of $\vec{H}$ is zero when ρ_m is zero, the magnetic field may be defined as the curl of an auxillary vector,

$$\vec{H} = \nabla \times \vec{A}, \tag{2.10}$$

where $\vec{A}$ is called the magnetic vector potential. After substituting (2.10) into (2.1) and noting that curl of $\vec{E}$ is proportional to the curl of $\vec{A}$ when $\vec{M}$ is zero, the electric scalar potential, Φ, is defined in terms of $\vec{E}$ and $\vec{A}$ as

$$-\nabla\Phi = \vec{E} + j\omega\mu\vec{A}. \tag{2.11}$$

The electric scalar potential and the magnetic vector potential allow for the solution of the electric and magnetic fields by one uncoupled equation, called the wave equation, rather than the two coupled curl equations (2.1) and (2.2). After substituting (2.10) and (2.11) into (2.2) and making use of a vector identity and the Lorentz gauge (Balanis, 1989),

$$\nabla \cdot \vec{A} = -j\omega\varepsilon\Phi, \tag{2.12}$$

the vector wave equation is found to be

$$\nabla^2 \vec{A} + k^2 \vec{A} = -\vec{J}. \tag{2.13}$$

Solving the vector wave equation for the magnetic vector potential due to $\vec{J}_s$, the free space solution is found to be

$$\vec{A}(\vec{r}) = \iint_S \vec{J}_s(\vec{r}\,')G(R)ds', \tag{2.14}$$

where the free space Green's Function, G, is given by

$$G(R) = \frac{e^{-jkR}}{4\pi R},\ R = |\vec{r} - \vec{r}'|. \tag{2.15}$$

The primed vector, $\vec{r}'$, defines the source coordinates, $\vec{r}$ defines the observation coordinates, and the wave number is $k = \omega\sqrt{\varepsilon_o \mu_o}$. The scattered electric field is then found from combining (2.11) and (2.12) to give

$$\vec{E}_s = -j\omega\mu_o \vec{A} - j\frac{1}{\omega\varepsilon_o}\nabla(\nabla \cdot \vec{A}), \tag{2.16}$$

where ε_o and μ_o are the permittivity and permeability of free space.

The final step in determining the EFIE is to combine (2.9) and (2.16) to relate the scattered and incident fields, giving

$$\hat{n} \times \frac{j}{\omega\varepsilon_o}\left(k^2 \vec{A} + \nabla(\nabla \cdot \vec{A})\right) = \hat{n} \times \vec{E}_i. \tag{2.17}$$

If $\vec{A}$ is replaced by (2.14), then (2.17) may be written as

$$\hat{n} \times \frac{j}{\omega\varepsilon}\left[\iint_S k^2 \vec{J}_s(\vec{r}')G(R)ds' + \nabla\left(\nabla \cdot \iint_S \vec{J}_s(\vec{r}')G(R)ds'\right)\right] = \hat{n} \times \vec{E}_i. \tag{2.18}$$

The second term on the left hand side of (2.18) can be further simplified by bringing the second ∇ operator inside the integral and integrating by parts. Finally, the remaining ∇ operator may also be brought inside the integral. After simplifying, (2.18) reduces to

$$\hat{n} \times \frac{j}{\omega\varepsilon_o}\iint_S \left[k^2 \vec{J}_s(\vec{r}')G(R) + \left(\nabla' \cdot \vec{J}_s(\vec{r}')\right)\nabla G(R)\right]ds' = \hat{n} \times \vec{E}_i, \tag{2.19}$$

where ∇' means that the "del" operator now works on the source coordinates, $\vec{r}'$. Equation (2.19) is the general electric field integral equation which will be used for the straight wire formulation later in this chapter, and also for the helix formulation in the next chapter. The above derivation was in part based on work presented by Stutzman and Thiele (1998) and Poggio and Miller (1987). A general derivation based on the vector Green's theorem, which does not assume a perfectly conducting surface, is also presented by Poggio and Miller.

2.2 Method of Moments

The Method of Moments (MoM) is a well known technique for solving linear equations. In antenna analysis, the MoM is used to convert the electric field integral equation into a matrix equation or system of linear equations. The matrix equation can then be solved for the current coefficients by LU decomposition, Gaussian elimination, or other techniques of linear algebra. The following development is based on the work by (Harrington, 1968).

The basic form of the equation to be solved by the Method of Moments is

$$L(u) = f \,, \tag{2.20}$$

where L is the linear operator, u is the unknown function, and f is the source or forcing function. In order to create the matrix equation, the unknown function is defined to be the sum of a set of known independent functions, u_n, called basis or expansion functions with unknown amplitudes, α_n,

$$u = \sum_n \alpha_n u_n \,. \tag{2.21}$$

Using the linearity of the operator, L, the unknown amplitudes can be brought out of the operator giving

$$\sum_n \alpha_n L\left(u_n\right) = f \,. \tag{2.22}$$

The unknown amplitudes cannot yet be determined because there are n unknowns, but one functional equation. A fixed set of equations are found by defining independent weighting or testing functions, w_m, which are integrated with (2.22) to give m different linear equations. The integration of the weighting functions with (2.22) may be written symbolically as the inner product of the two functions, giving

$$\sum_n \alpha_n \left\langle w_m, L\left(u_n\right)\right\rangle = \left\langle w_m, f \right\rangle, \tag{2.23}$$

where the inner product[1], $\langle a,b\rangle$, is defined to be the integral of the two functions over the domain of the linear operator. Now there are an equal number of unknowns and independent equations, which allow for the solution of the unknown amplitudes, α_n.

[1] The form of the inner product for real functions is used, though strictly speaking the functions may be complex. The range of complex variation is sufficiently small to allow this use of the form.

For antenna problems, the matrix equation of (2.23) is usually written in a form similar to Ohm's Law (Stutzman and Thiele, 1981),

$$\left[Z_{m,n}\right]\left[I_n\right]=\left[V_m\right]. \tag{2.24}$$

The generalized impedance matrix is given by $\left[Z_{m,n}\right]=\left[\left\langle w_m, L\left(u_n\right)\right\rangle\right]$, the generalized current matrix is given by $\left[I_n\right]=\left[\alpha_n\right]$, and the generalized voltage matrix is given by $\left[V_m\right]=\left[\left\langle w_m, f\right\rangle\right]$. The generalized matrices may need to be scaled to obtain the same units as the counterparts in Ohm's Law.

2.3 Straight Wire Formulation

The electric field integral equation for straight wire geometries has been studied in great depth for many years. One of the most well known forms of the EFIE was developed by Pocklington (1897). The derivation of Pocklington's integral equation for straight wires is similar to that of Sec. 2.1. The straight wire geometry of Fig. 2.2 is used in the following formulation. For this geometry, the Lorentz gauge along the wire length, ℓ, reduces to

$$\Phi=-\frac{1}{j\omega\varepsilon_o}\frac{\partial}{\partial\ell}A_\ell, \tag{2.25}$$

and the scattered electric field of (2.16) becomes

$$E_\ell=-j\omega\mu_o A_\ell-\frac{\partial}{\partial\ell}\Phi, \tag{2.26}$$

where the ℓ subscripts indicate the component of the vectors in the $\hat{\ell}$ direction. After taking the derivative of (2.25) and substituting the result into (2.26), the electric field may be written as

$$E_\ell=\frac{1}{j\omega\varepsilon_o}\left[k^2A_\ell+\frac{\partial^2}{\partial\ell^2}A_\ell\right]. \tag{2.27}$$

Making use of the thin wire approximation, which states that the current around the circumference of the wire is uniform and the axially directed electric field is to be estimated along the axis of the current in the $\hat{\ell}$ direction, the vector potential, A_ℓ, is given by

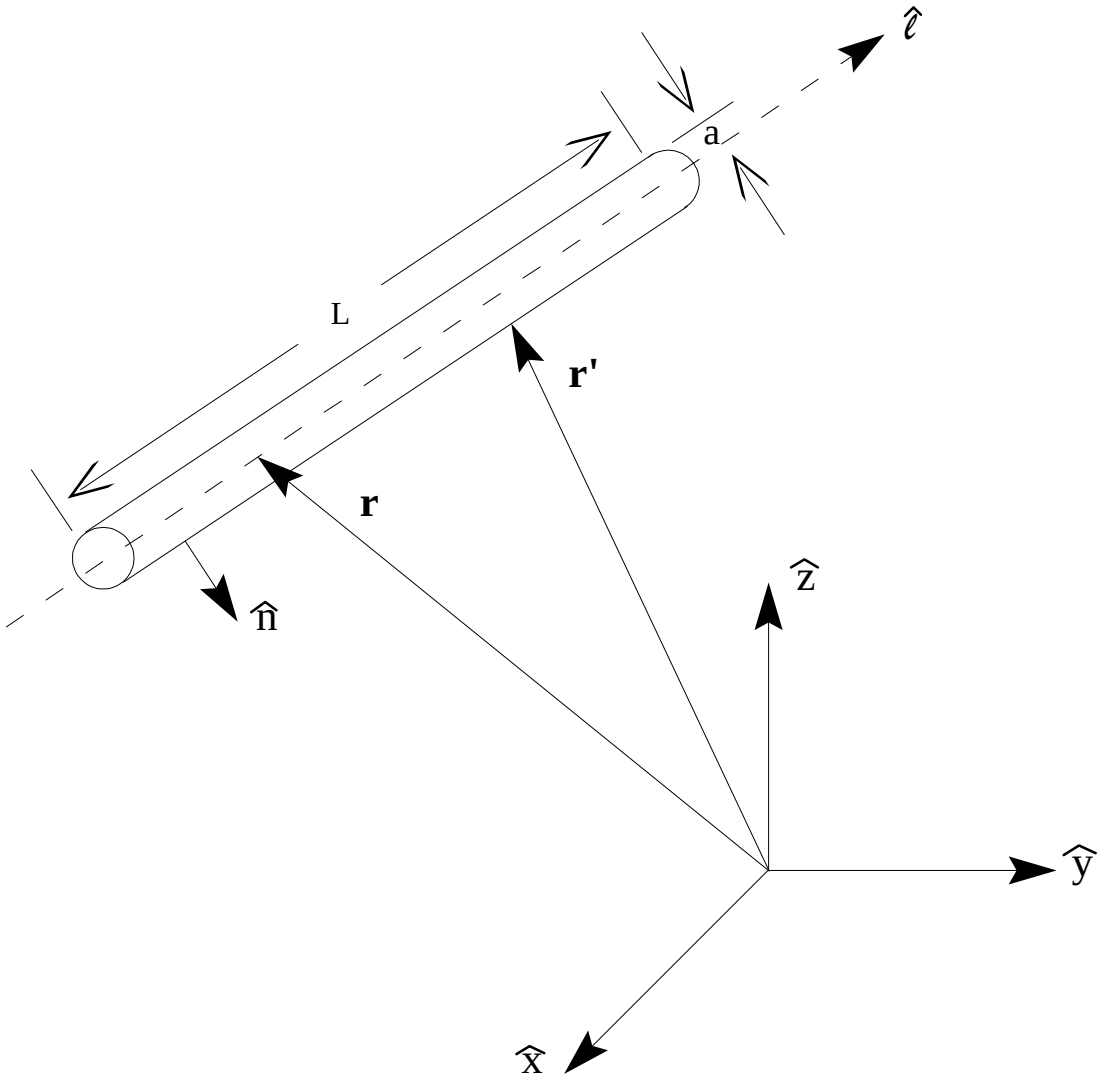

Figure 2.2 Straight wire geometry.

$$A_\ell = \int_{-L/2}^{L/2} I(\ell')G(R)d\ell',\ R = \sqrt{(\ell-\ell')^2 + a^2}\ . \tag{2.28}$$

Finally, combining (2.27), (2.28), and the electric field boundary condition at the surface of the wire, (2.9), Pocklington's electric field integral equation is given by

$$\frac{j}{\omega\varepsilon_o}\int_{-L/2}^{L/2} I(\ell')\left[\frac{\partial^2}{\partial\ell^2}G(R) + k^2 G(R)\right]d\ell' = E_i^\ell\ , \tag{2.29}$$

where E_i^ℓ is the part of the incident electric field directed along the $\hat{\ell}$ axis. Note that, in general, Pocklington's equation, (2.29), is not valid. The use of the thin wire approximation allows the $\left[\frac{\partial^2}{\partial\ell^2} + k^2\right]$ term to be brought inside the integral since the second derivative is now defined.

As an example, consider a center fed dipole antenna in the $\hat{z}$ direction. Using the Method of Moments to solve the problem, the current is expanded using piece-wise sinusoidal basis functions giving

$$I(z') = \sum_n I_n \begin{cases} \dfrac{\sin k\left(z' - z_{n-1}\right)}{\sin k\left(z_n - z_{n-1}\right)}, & z_{n-1} \le z' < z_n \\ \dfrac{\sin k\left(z_{n+1} - z'\right)}{\sin k\left(z_{n+1} - z_n\right)}, & z_n \le z' < z_{n+1}\ , \\ 0, & \textit{otherwise} \end{cases} \tag{2.30}$$

and the weighting functions are pulses one segment wide as shown if Fig. 2.3. The incident electric field is approximated by the delta gap source model which assumes that the incident electric field is due to the applied voltage across a small gap in the antenna, of width δ approaching zero, and is confined to that gap.

To prepare Pocklington's integral equation for solution, the first term of (2.29) will be integrated by parts twice where the following substitutions will be used, $\frac{\partial}{\partial\ell}G(R) = -\frac{\partial}{\partial\ell'}G(R)$ and $\frac{\partial^2}{\partial\ell^2}G(R) = \frac{\partial^2}{\partial\ell'^2}G(R)$ with $R = \sqrt{(\ell-\ell')^2 + a^2}$. The actual equation that will be solved is now given by

$$\frac{j}{\omega\varepsilon_o}\int_{-L/2}^{L/2}\left[\frac{\partial^2}{\partial z'^2}I(z') + k^2 I(z')\right]G(R)dz' = E_i^z,\ R = \sqrt{(z-z')^2 + a^2} \tag{2.31}$$

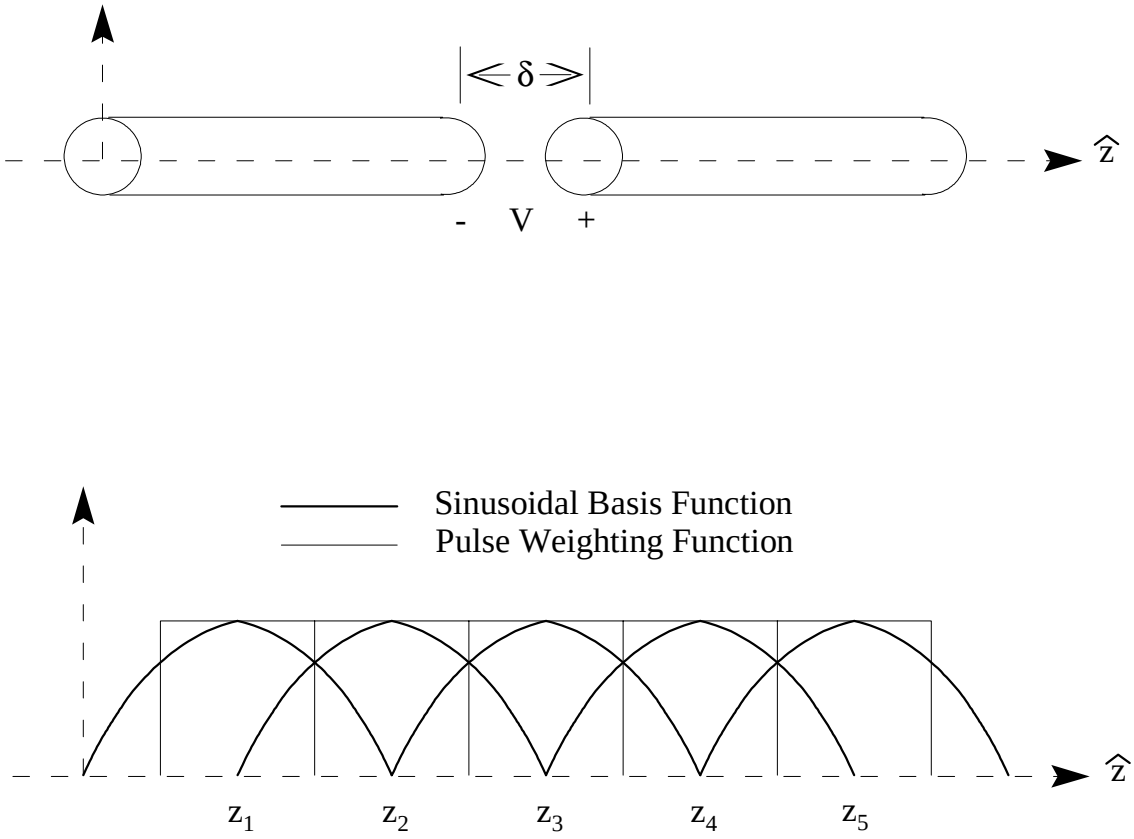

Figure 2.3 Geometry, basis function, and weighting function for straight wire example.

where it is assumed the antenna is $\hat{z}$ directed and the approximation of $I(z')$ in (2.30) is to be used. Incorporating the piece-wise sinusoidal basis functions, the pulse weighting functions, and the delta gap source model into (2.31), gives

$$\sum_n I_n \frac{j}{\omega\varepsilon_o} \int_{z_m-\frac{\Delta}{2}}^{z_m+\frac{\Delta}{2}} \int_{z_n-\Delta^+}^{z_n+\Delta^+} \frac{k}{\sin k\Delta}\left[\delta(z'-z_{n+1})+\delta(z'-z_{n-1})-2\delta(z'-z_n)\cos k\Delta\right]G(R)dz'dz = \int_{z_m-\frac{\Delta}{2}}^{z_m+\frac{\Delta}{2}} \frac{V_{ms}}{\Delta}\delta(z-z_{ms})dz \tag{2.32}$$

where Δ is one segment length, z_n is $n\Delta$ from the origin along the $\hat{z}$ axis, z_{ms} is the location of the m^{th} source, and V_{ms} is the voltage of the m^{th} source. The notation, Δ^+, has been used to indicate that the end points are to be considered in the interval. Finally, evaluating the integral of the delta functions on the left-hand side of (2.32) gives

$$\sum_n I_n \frac{j}{\omega\varepsilon_o}\frac{k}{\sin k\Delta}\int_{z_m-\frac{\Delta}{2}}^{z_m+\frac{\Delta}{2}} G(R_{n+1})+G(R_{n-1})-2G(R_n)\cos k\Delta dz = \int_{z_m-\frac{\Delta}{2}}^{z_m+\frac{\Delta}{2}} \frac{V_{ms}}{\Delta}\delta(z-z_{ms})dz \tag{2.33}$$

where $R_n = \sqrt{(z-z_n)^2+a^2}$.

To illustrate the solution of (2.33), consider a resonant dipole antenna with a length of 0.47λ, a radius of 0.005λ, 6 segments, and a source voltage of 1 volt. The segment length is equal to the dipole length divided by the number of segments, which for this example is 0.0783λ. The number of unknowns is 5, one less than the number of segments because each basis function spans 2 segments. It is convenient to choose an odd number of unknowns (or even number of segments) so that the antenna may be feed at the center unknown. If an even number of unknowns are chosen, half of the desired source voltage may be placed across each of the two center elements to obtain the same effect.

After evaluating (2.33) for the above specifications, the impedance matrix is

$$Z = \begin{bmatrix} 488.5\angle -89.4° & 256.6\angle 88.9° & 32.3\angle 82.1° & 9.2\angle 64.7° & 4.5\angle 43.2° \\ 256.6\angle 88.9° & 488.5\angle -89.4° & 256.6\angle 88.9° & 32.3\angle 82.1° & 9.2\angle 64.7° \\ 32.3\angle 82.1° & 256.6\angle 88.9° & 488.5\angle -89.4° & 256.6\angle 88.9° & 32.3\angle 82.1° \\ 9.2\angle 64.7° & 32.3\angle 82.1° & 256.6\angle 88.9° & 488.5\angle -89.4° & 256.6\angle 88.9° \\ 4.5\angle 43.2° & 9.2\angle 64.7° & 32.3\angle 82.1° & 256.6\angle 88.9° & 488.5\angle -89.4° \end{bmatrix}$$

and the voltage vector is

$$V = \begin{bmatrix} 0 \\ 0 \\ 1\angle 0° \\ 0 \\ 0 \end{bmatrix}.$$

Now, solving for the current vector gives

$$I = 10^{-3} \begin{bmatrix} 8.1\angle -1.0° \\ 13.0\angle 1.9° \\ 14.8\angle 7.5° \\ 13.0\angle 1.9° \\ 8.1\angle -1.0° \end{bmatrix},$$

for an input impedance of $66.9 - j8.8$ ohms. Note that the impedance matrix is symmetric and the voltage and current vectors are symmetric about the center element. The voltage and current symmetry is a result of the antenna being center fed with a constant segment length. The symmetry of the impedance matrix is similarly due to the straight wire geometry and constant segment length chosen for the example. Once the first row of the impedance matrix is calculated, the rest of the matrix can be generated from the following formula (Stutzman and Thiele, 1998),

$$\left[Z_{m,n}\right] = \left[Z_{1,|m-n|+1}\right] \quad m \geq 2, n \geq 1. \tag{2.34}$$

Such matrices are called Toeplitz matrices. A considerable amount of computation work and time can be saved when the impedance matrix is a Toeplitz matrix. Some additional time can be saved when computing the current vector for a Toeplitz impedance matrix. In the next chapter, the impedance matrix for the helix antenna will also be shown to have a Toeplitz form.

A perfectly resonant half-wave dipole is typically found to have an input impedance of $72 + j0$ ohms, which varies slightly from that obtained in the above example. The difference is caused by the small number of segments used in the example. Six segments were chosen so that the matrices could be displayed in a relatively small amount of space, but a better answer is obtained if more segments were used. For example, if 12 segments are used the input impedance is $71.3 - j1.8$ ohms, which is very close to the expected resonant value. Fig. 2.4 shows that the input impedance converges to approximately $77 + j5$ ohms and the input admittance converges to approximately $0.013 - j0.00084$ siemens for 60 segments. The input admittance plot is interesting because it shows slightly better convergence than the input impedance plot. The thin wire approximation begins to break down as the segment length approaches the radius of the

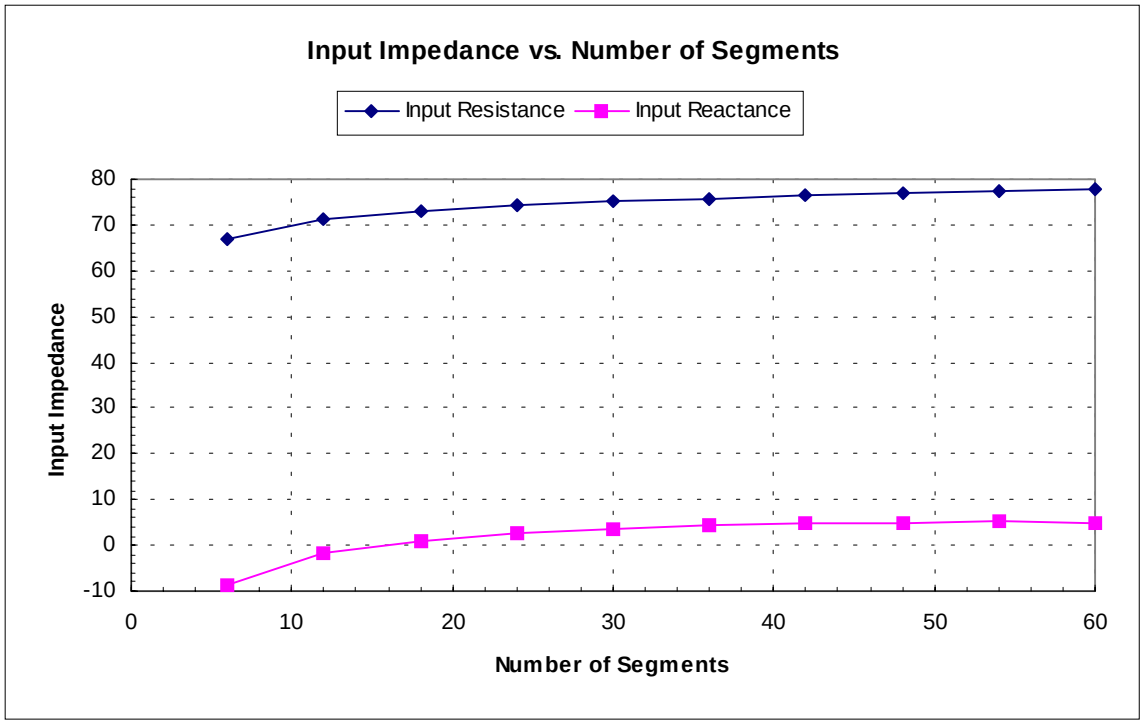

(a) Input impedance.

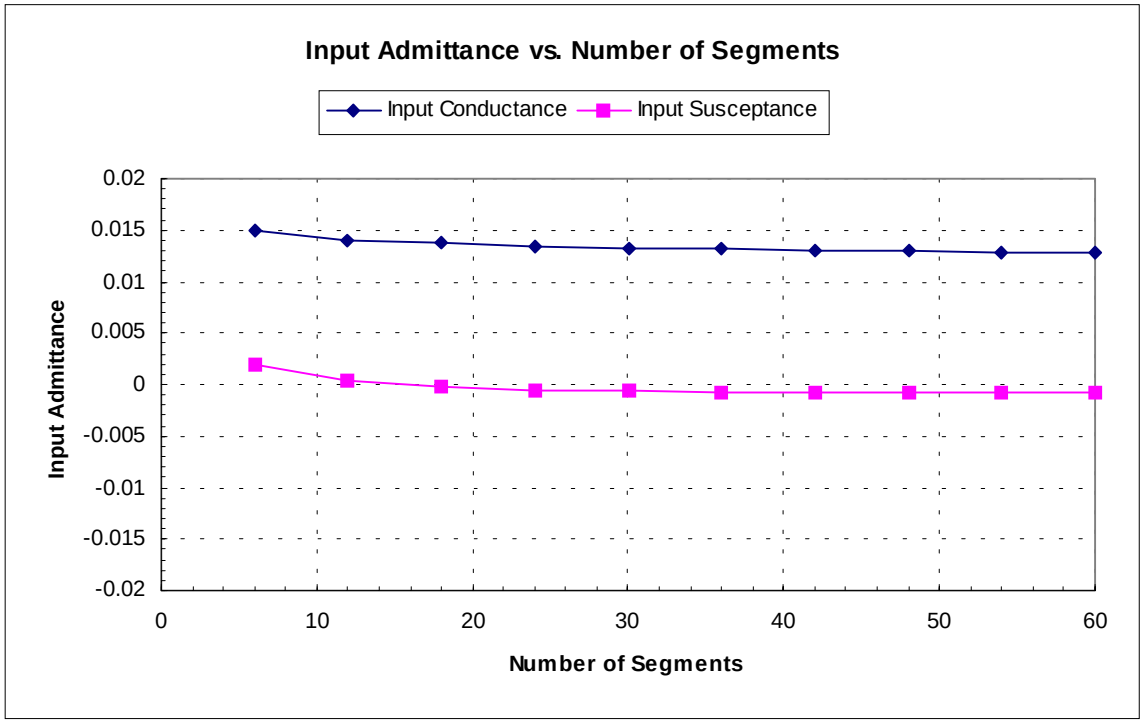

(b) Input admittance.

Figure 2.4 Input impedance and admittance vs. number of segments. $L = 0.47\lambda$, $a = 0.005\lambda$

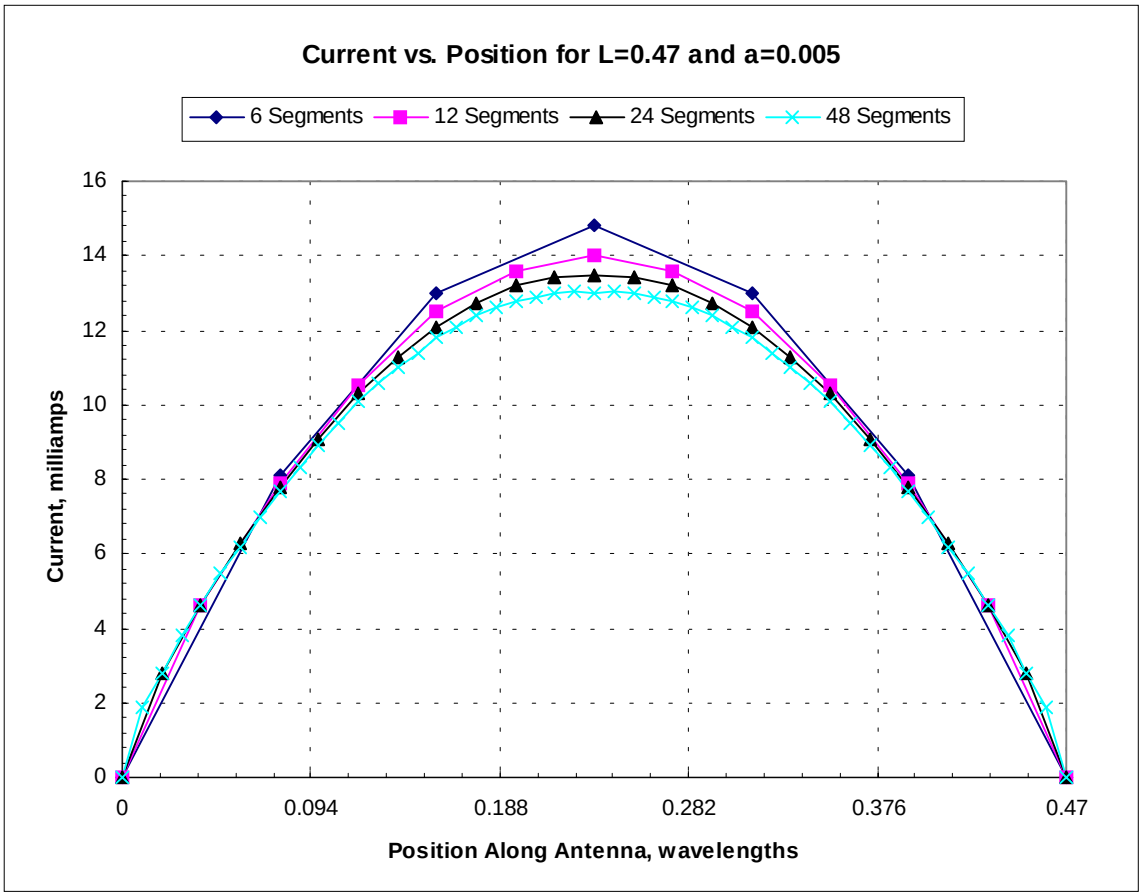

Figure 2.5 Current distribution vs. position. $L = 0.47\lambda$, $a = 0.005\lambda$

wire, a. For 100 segments, $\Delta = 0.94a$, and the input impedance is $80.0 + j0.74$ ohms and the input admittance is $0.012 + j0.00012$ siemens, which both show divergence from the values of Fig. 2.4. The effect of increasing the number of segments on the current distribution is shown in Fig. 2.5. As the number of segments is increased, the current maximum decreases and begins to form a small dip as expected, but if only an estimate of the current is needed even the 6 segment case produces good results. This dip is the result of multiple effects caused by the increase in unknowns. These effects include an increase in the effective length of the dipole and a shunt knife edge capacitance at the feed as the number of unknowns increases.

The dependence of the answer on the number of unknowns (or segments) is expected when using the Method of Moments, since the expansion functions more closely approximate the true current distribution as the number of unknowns is increased. In practice, the answer will usually appear to converge as the number of unknowns is increased, but may begin to breakdown if too many unknowns are used due to numerical and modeling constraints on the solution algorithms. It is also possible to obtain slightly different results and have various convergence speeds depending upon the expansion and weighting functions used in the problem. (Miller and Deadrick, 1975)

Pocklington's integral equation may be the most commonly used form of the electric field integral equation, but there are other forms that may be used to solve wire antenna problems. One such form of the EFIE was developed by Hallen (1938). Hallen's integral equation is found by solving the vector wave equation, giving

$$\int_{-L/2}^{L/2} I(\ell')G(R)d\ell' = -\frac{j}{\omega\varepsilon_o}\left(C_1\cos k\ell + C_2\sin k\ell + \frac{V_T}{2}\sin k|\ell|\right),$$

$$R = \sqrt{(\ell-\ell')^2 + a^2}\ . \tag{2.35}$$

The unknowns, C_1 and C_2, are found from making the current go to zero at the ends of the wire, and V_T is the voltage applied at the center of the antenna. The Hallen formulation with point matching is equivalent to the Pocklington formulation with piecewise sinusoidal testing functions, the latter including the Green's function of the differential operator (Wilton and Butler, 1976). Hallen's formulation is not as common as Pocklington's equation because it is more difficult to generalize for bent wire structures and will not be pursued any further. The next chapter develops another form of the EFIE, which can be used for general wire antenna structures.

3. Helix Antenna Theory

This chapter develops the theory used for a Moment Method program to solve for the currents on a helix antenna. First, the geometry and equations necessary to describe a helical structure will be presented. The electric field integral equation derived in Section 2.1 will be applied to the helix and setup to solve by the Method of Moments. A feed will also be introduced, consisting of straight wires connecting the helix and a perfect ground. Triangle basis functions and pulse weighting functions will be used on the straight wires of the feed and the helix antenna when implementing the Method of Moments. For the helix, both the basis and weighting functions will follow the contour of the helical structure.

3.1 Helix Description

For this thesis, the helix is oriented along the z axis, perpendicular to perfect ground lying in the $xy-$plane. The parameters and geometry used to describe the helical structure are shown in Fig. 3.1. The starting height of the helix is given by z_o, ρ is the radius of the helix, L is the length of one turn, α is the pitch angle, S is the spacing between turns, $\hat{\ell}$ is the tangential unit vector describing the contour of the helix, and a is the radius of the wire used to wind the helix. Fig. 3.1 also shows a schematic of one turn of the helix if it were unwound (Stutzman and Thiele, 1981). This schematic helps in understanding the relationships between the parameters.

The helical contour can be described by the vector,

$$\bar{r} = \hat{x}x + \hat{y}y + \hat{z}\left(z + z_o\right), \tag{3.1}$$

which points from the origin to any point on the helix. The x and y coordinates are given by

$$x = \rho\cos\left(\frac{2\pi}{S}\left(z - z_o\right)\right) \tag{3.2}$$

and

$$y = \rho\sin\left(\frac{2\pi}{S}\left(z - z_o\right)\right). \tag{3.3}$$

The spacing between turns can be written as $S = L\sin\alpha$, and the z coordinate is given by $z = \ell\sin\alpha$, where ℓ is the distance along the helix in the $\hat{\ell}$ direction. Combining the above relationships with (3.1) gives

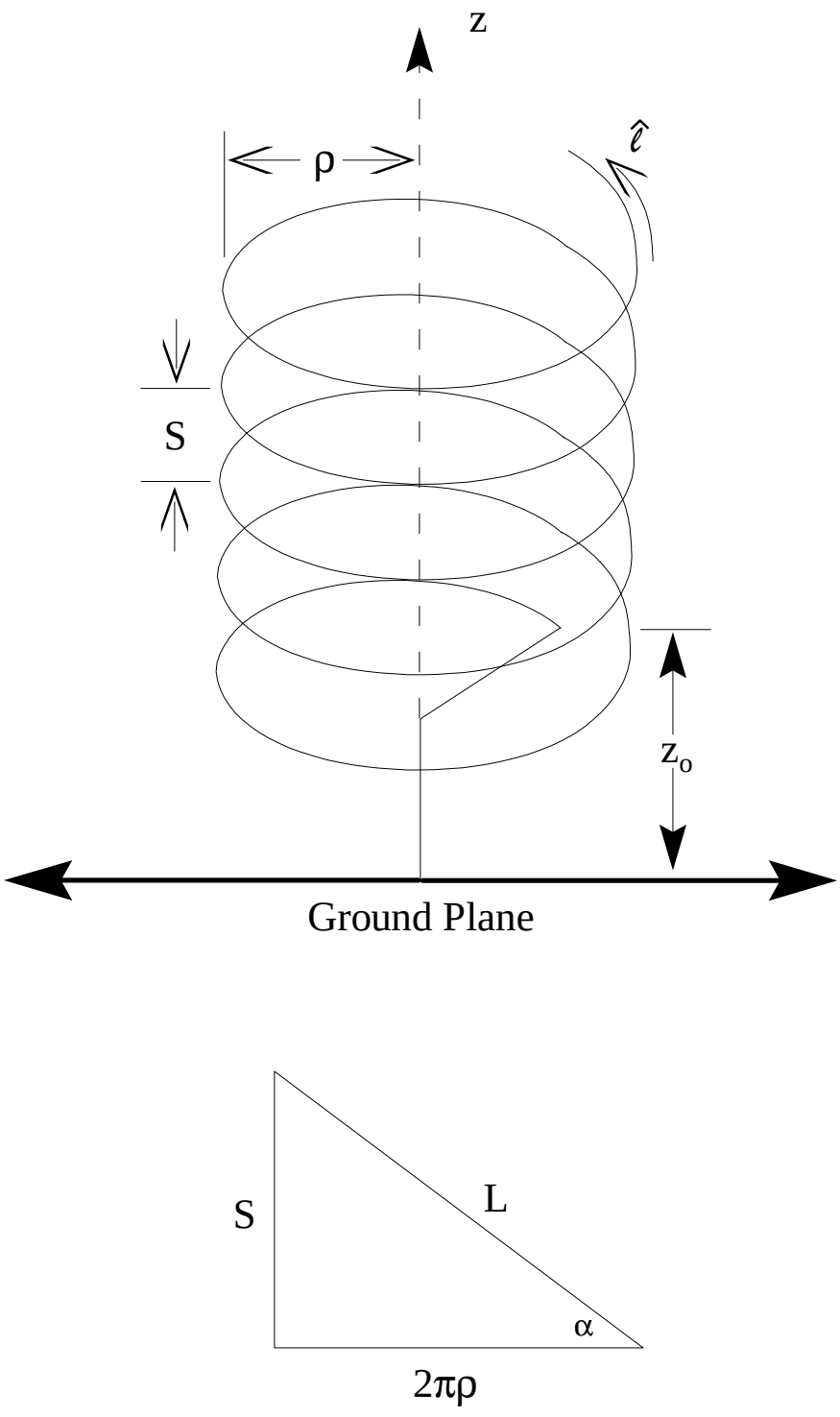

Figure 3.1 Helix geometry.

$$\vec{r} = \hat{x}\rho\cos\left(\frac{2\pi}{L}\ell\right) + \hat{y}\rho\sin\left(\frac{2\pi}{L}\ell\right) + \hat{z}\left(\ell\sin\alpha + z_o\right), \tag{3.4}$$

which describes any point on the helix. The unit vector, $\hat{\ell}$, which describes the contour of the helix is defined by $\hat{\ell} = \frac{\partial}{\partial\ell}\vec{r}$. Recognizing from Fig. 3.1 that $\rho = \frac{L\cos\alpha}{2\pi}$, the unit vector is given by

$$\hat{\ell} = -\hat{x}\cos\alpha\sin\left(\frac{2\pi}{L}\ell\right) + \hat{y}\cos\alpha\cos\left(\frac{2\pi}{L}\ell\right) + \hat{z}\sin\alpha\,. \tag{3.5}$$

Finally, the unit vector, $\hat{\ell}$, can be written in cylindrical coordinates by using $\phi = \frac{2\pi}{L}\ell$ and $\hat{\phi} = -\hat{x}\sin\phi + \hat{y}\cos\phi$, giving

$$\hat{\ell} = \hat{\phi}\cos\alpha + \hat{z}\sin\alpha\,. \tag{3.6}$$

Equations (3.4) and (3.6) will be used in the development of the electric field integral equation for the helix in the next section.

3.2 Helix Antenna Formulation

The solution for the currents on the helix antenna begins with the electric field integral equation derived in Section 2.1,

$$\hat{n}\times\frac{j}{\omega\varepsilon_o}\iint_S\left[k^2\vec{J}_s(\vec{r}\,')G(R) + \left(\nabla'\cdot\vec{J}_s(\vec{r}\,')\right)\nabla G(R)\right]ds' = \hat{n}\times\vec{E}_i\,. \tag{2.19}$$

As in the straight wire example presented in the previous chapter, the thin wire approximation will be used for the helix. This means that the surface current, $\vec{J}_s(\vec{r}\,')$, is approximated as a line current given by $I(\ell')\hat{\ell}'$, where $\hat{\ell}'$ is defined at the source point and follows the contour of the helix. Similarly, the ∇' operator reduces to $\hat{\ell}'\frac{\partial}{\partial\ell'}$. Equation (2.19) can now be written as

$$\hat{\ell}\cdot\frac{j}{\omega\varepsilon_o}\int_{\ell'}\left[\hat{\ell}'k^2I(\ell')G(R) + \left(\frac{\partial}{\partial\ell'}I(\ell')\right)\nabla G(R)\right]d\ell' = \hat{\ell}\cdot\vec{E}_i\,, \tag{3.7}$$

where the $\hat{n}\times$ has been replaced by the dot product with $\hat{\ell}$. The distance between the source and observation points, R, is based on the thin wire approximation and is a function of ℓ and ℓ' which will be derived later in this section.

Now, applying the Method of Moments to (3.7), the current is approximated as a sum of expansion functions giving

$$I(\ell') = \sum_n I_n u_n(\ell'), \tag{3.8}$$

and the weighting function is represented by $w_m(\ell)$. Combining the expansion and weighting functions with (3.7) gives

$$\begin{aligned} &\frac{j}{\omega\varepsilon_o}\sum_n I_n\left[k^2\int_\ell w_m(\ell)\int_{\ell'}\left(\hat{\ell}\cdot\hat{\ell}'\right)u_n(\ell')G(R)d\ell' d\ell\right. \\ &\left.+\int_\ell w_m(\ell)\int_{\ell'}\left(\hat{\ell}\cdot\nabla G(R)\right)\frac{\partial}{\partial\ell'}u_n(\ell')d\ell' d\ell\right] = \int_\ell w_m(\ell)\hat{\ell}\cdot\vec{E}_i d\ell. \end{aligned} \tag{3.9}$$

Finally, substituting $\hat{\ell}\cdot\nabla G(R) = \frac{\partial}{\partial\ell}G(R)$ into (3.9) gives

$$\begin{aligned} &\frac{j}{\omega\varepsilon_o}\sum_n I_n\left[k^2\int_\ell w_m(\ell)\int_{\ell'}\left(\hat{\ell}\cdot\hat{\ell}'\right)u_n(\ell')G(R)d\ell' d\ell\right. \\ &\left.+\int_\ell w_m(\ell)\frac{\partial}{\partial\ell}\int_{\ell'}G(R)\frac{\partial}{\partial\ell'}u_n(\ell')d\ell' d\ell\right] = \int_\ell w_m(\ell)\hat{\ell}\cdot\vec{E}_i d\ell. \end{aligned}, \tag{3.10}$$

where the integral equation depends only on ℓ and ℓ' with their corresponding unit vectors. Equation (3.10) is a general equation that applies to any thin wire antenna geometry, not just the helix, by defining the appropriate wire contour $\hat{\ell}$.

The basis function chosen for the helix antenna problem is a two segment wide triangle function centered about the junction between the two segments given by

$$u_n(\ell') = T_n(\ell') = \begin{cases} 1-\dfrac{|\ell'-n\Delta|}{\Delta}, & |\ell'-n\Delta| < \Delta \\ 0, & \textit{otherwise} \end{cases}, \tag{3.11}$$

where Δ is the segment length. The weighting function is a one segment wide pulse function also centered about the junction between the two segments defined as

$$w_m(\ell) = P_m(\ell) = \begin{cases} 1, & |\ell - m\Delta| < \dfrac{\Delta}{2} \\ 0, & otherwise \end{cases}. \tag{3.12}$$

Note that both the basis and weighting functions follow the contour of the helix described by the unit vector, $\hat{\ell}$. Fig. 3.2 shows the geometry for the helix antenna and the orientation of the basis and weighting functions. The helix is assumed to have a starting angle of $\phi = 0$, and the origin of the ℓ-axis is at the bottom of the helix as shown.

Now, substituting the triangle basis function and pulse weighting function into (3.10) gives

$$\begin{aligned} &\frac{j}{\omega\varepsilon_o}\sum_n I_n\Bigg[k^2\int_{\ell_m}\int_{\ell'}\left(\hat{\ell}\cdot\hat{\ell}'\right)T_n(\ell')G(R)d\ell' d\ell \\ &+\int_{\ell_m}\frac{\partial}{\partial\ell}\int_{\ell'}G(R)\frac{\partial}{\partial\ell'}T_n(\ell')d\ell' d\ell\Bigg] = \int_{\ell_m}\hat{\ell}\cdot\vec{E}_i d\ell. \end{aligned} \tag{3.13}$$

where the integral over ℓ_m represents the integral over the extent of the m^{th} pulse weighting function and the integral over ℓ' represents the integral over the extent of the antenna, but is bounded by the n^{th} triangle basis function, $T_n(\ell')$. The second term on the left hand side of (3.13) can be further simplified by recognizing that $\int_a^b \frac{\partial}{\partial x} f(x,y)dx = f(x,y)\Big|_a^b$ which gives

$$\begin{aligned} &\frac{j}{\omega\varepsilon_o}\sum_n I_n\Bigg[k^2\int_{\ell_m}\int_{\ell'}\left(\hat{\ell}\cdot\hat{\ell}'\right)T_n(\ell')G(R)d\ell' d\ell \\ &+\left(\int_{\ell'}G(R)\frac{\partial}{\partial\ell'}T_n(\ell')d\ell'\right)\Bigg|_{\ell_m^-}^{\ell_m^+}\Bigg] = \int_{\ell_m}\hat{\ell}\cdot\vec{E}_i d\ell. \end{aligned} \tag{3.14}$$

The derivative of the triangle basis function can be represented by the difference of two pulse functions,

$$\frac{\partial}{\partial\ell'}T_n(\ell') = \frac{1}{\Delta}\left[P_n^+(\ell') - P_n^-(\ell')\right]. \tag{3.15}$$

The pulse functions, $P_n^+(\ell')$ and $P_n^-(\ell')$, represent the positive and negative sloped sides of the triangle function respectively, and are given by

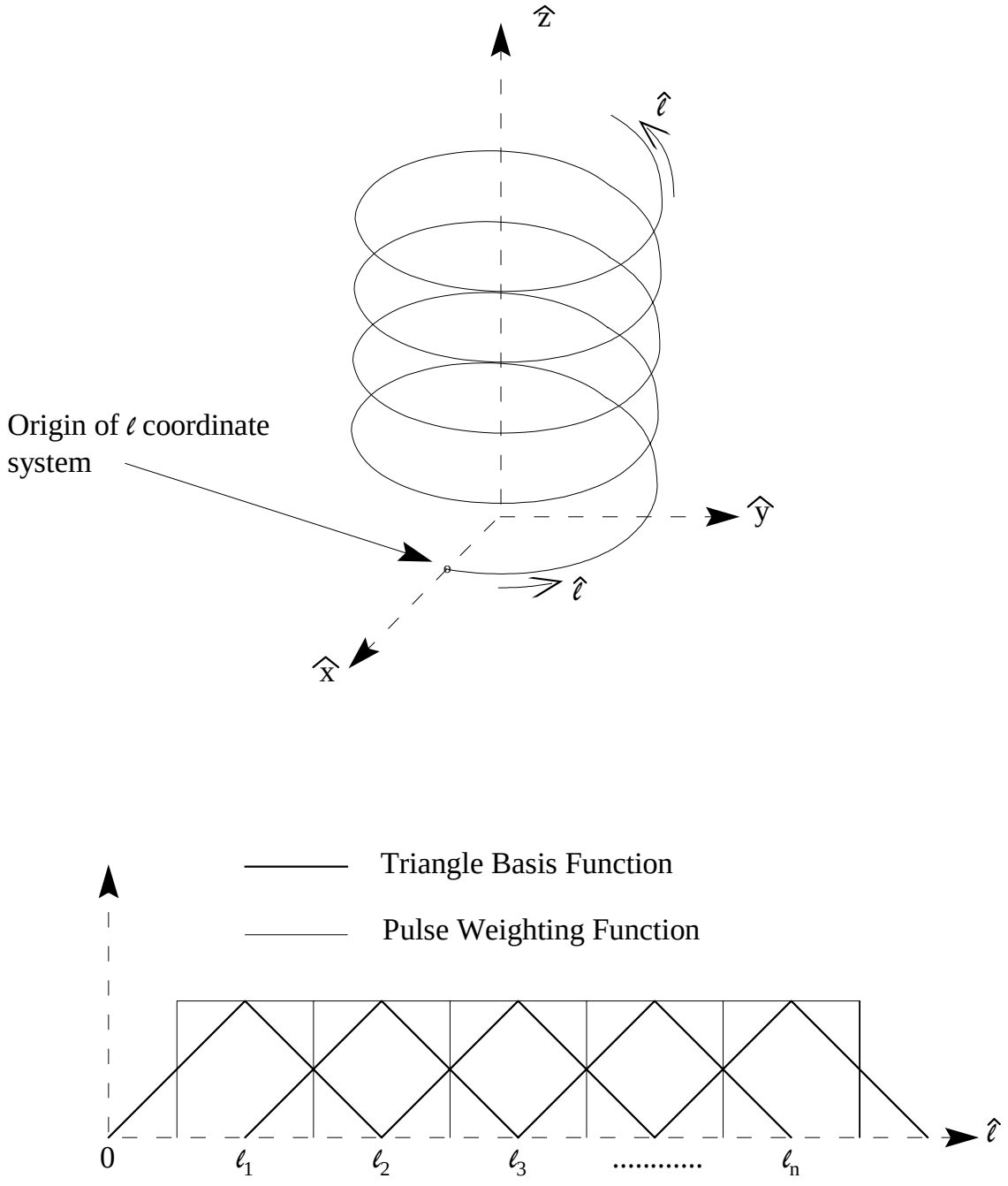

Figure 3.2 Helix coordinate system, basis function, and weighting function.

$$P_n^+(\ell') = \begin{cases} 1, & \left|\ell' - n\Delta + \dfrac{\Delta}{2}\right| < \dfrac{\Delta}{2} \\ 0, & otherwise \end{cases} \tag{3.16}$$

and

$$P_n^-(\ell') = \begin{cases} 1, & \left|\ell' - n\Delta - \dfrac{\Delta}{2}\right| < \dfrac{\Delta}{2} \\ 0, & otherwise \end{cases}. \tag{3.17}$$

Finally, substituting (3.15) into (3.14) gives

$$\begin{aligned} &\frac{j}{\omega\varepsilon_o}\sum_n I_n\left[k^2\int_{\ell_m}\int_{\ell'}\left(\hat{\ell}\cdot\hat{\ell}'\right)T_n(\ell')G(R)d\ell'\,d\ell\right. \\ &\left.+\left(\int_{\ell'}\frac{G(R)}{\Delta}\left[P_n^+(\ell')-P_n^-(\ell')\right]d\ell'\right)\Bigg|_{\ell_m^-}^{\ell_m^+}\right] = \int_{\ell_m}\hat{\ell}\cdot\vec{E}_i\,d\ell. \end{aligned} \tag{3.18}$$

The right hand side of (3.18) will be determined by using the delta gap source model that was described in Section 2.3 for the straight wire problem. Replacing the right hand side of (3.18) with the delta gap source model from Eq. (2.32) gives

$$\begin{aligned} &\frac{j}{\omega\varepsilon_o}\sum_n I_n\left[k^2\int_{\ell_m}\int_{\ell'}\left(\hat{\ell}\cdot\hat{\ell}'\right)T_n(\ell')G(R)d\ell'\,d\ell\right. \\ &\left.+\left(\int_{\ell'}\frac{G(R)}{\Delta}\left[P_n^+(\ell')-P_n^-(\ell')\right]d\ell'\right)\Bigg|_{\ell_m^-}^{\ell_m^+}\right] = \int_{\ell_m}\frac{V_{ms}}{\Delta}\delta\left(\ell - s_m\right)d\ell. \end{aligned} \tag{3.19}$$

where V_{ms} is the voltage of the m^{th} source and s_m is the location of the m^{th} source. Equation (3.19) is the final form of the electric field integral equation for the helix that will be presented here. A substitution of variables, $\ell - \ell'$, was used in the actual program to make the integration a bit easier to code, but is not necessary for understanding the formulation presented in this section. However, before equation (3.19) can be implemented the dot product, $\left(\hat{\ell}\cdot\hat{\ell}'\right)$, and the distance between the source and observation points, R, must be defined.

First, consider the dot product term. The unit vector which describes the contour of the helix was defined in Section 3.1 and is given by

$$\hat{\ell} = -\hat{x}\cos\alpha\sin\left(\frac{2\pi}{L}\ell\right) + \hat{y}\cos\alpha\cos\left(\frac{2\pi}{L}\ell\right) + \hat{z}\sin\alpha\,. \tag{3.5}$$

In equation (3.18), the $\hat{\ell}$ unit vector describes the helix for the observation points and the $\hat{\ell}'$ unit vector similarly describes the helix for the source points. The source unit vector is defined in the same manner as (3.5), giving

$$\hat{\ell}' = -\hat{x}\cos\alpha\sin\left(\frac{2\pi}{L}\ell'\right) + \hat{y}\cos\alpha\cos\left(\frac{2\pi}{L}\ell'\right) + \hat{z}\sin\alpha\,. \tag{3.20}$$

The dot product of (3.5) and (3.20) is then given by

$$\left(\hat{\ell}\cdot\hat{\ell}'\right) = \cos^2\alpha\cos\left(\frac{2\pi}{L}(\ell-\ell')\right) + \sin^2\alpha\,. \tag{3.21}$$

The distance between the source and observation points is an approximate length based on the thin wire approximation. The distance between the center of the wire at the source points and the center of the wire at the observation points is defined to be $R_o = |\vec{r} - \vec{r}'|$. The total distance, R, is then approximated by

$$R = \sqrt{R_o^2 + a^2}\,, \tag{3.22}$$

where, a, is the radius of the wire used to construct the helix. To determine R_o, the vectors to the source and observation points are needed. The vector to the observation point was defined in Section 3.1 as

$$\vec{r} = \hat{x}\rho\cos\left(\frac{2\pi}{L}\ell\right) + \hat{y}\rho\sin\left(\frac{2\pi}{L}\ell\right) + \hat{z}\left(\ell\sin\alpha + z_o\right), \tag{3.5}$$

and the vector to the source point is defined similarly as

$$\vec{r}' = \hat{x}\rho\cos\left(\frac{2\pi}{L}\ell'\right) + \hat{y}\rho\sin\left(\frac{2\pi}{L}\ell'\right) + \hat{z}\left(\ell'\sin\alpha + z_o\right). \tag{3.23}$$

The distance between the source and observation points is given by

$$R_0 = \sqrt{\left(\frac{L\cos\alpha}{\pi}\right)^2\sin^2\left(\frac{\pi}{L}(\ell-\ell')\right) + (\ell-\ell')^2\sin^2\alpha}\,. \tag{3.24}$$

The material presented in this section is sufficient for the calculation of the currents on a helix in free space. The addition of feed wires and a perfect ground plane will be discussed in the following two sections.

3.3 Feed Wire Formulation

In this section, the theory for the addition of feed wires to the helix antenna will be developed, allowing more realistic antenna geometries to be analyzed. The connection terms at the junction of two wires, as well as the terms where the source and observation points are on different wires will also be presented.

As shown in Fig. 3.1, the feed wires used in this thesis are straight wires. The same triangle basis and pulse weighting functions that were used in the previous section for the helix will also be used for the straight feed wires rather than the sinusoidal basis and pulse weighting functions used in the previous chapter for the straight wire example. For multiple wire structures, the sinusoidal-pulse combination no longer has a computational advantage over the triangle-pulse combination. Eq. (3.19), which was the final equation for the helix, is also applicable to the straight wire problem, but with different definitions of $\hat{\ell}$ and R. If the ends of the wire are described by the coordinates (x_1, y_1, z_1) and (x_2, y_2, z_2), then the unit vector along the wire is given by

$$\hat{\ell} = \frac{(x_2 - x_1)\hat{x} + (y_2 - y_1)\hat{y} + (z_2 - z_1)\hat{z}}{\sqrt{(x_2 - x_1)^2 + (y_2 - y_1)^2 + (z_2 - z_1)^2}}. \tag{3.25}$$

Unlike the helix, both $\hat{\ell}$ and $\hat{\ell}'$ are in the same direction for a single straight wire giving a dot product of unity, $(\hat{\ell} \cdot \hat{\ell}') = 1$. The distance between the source and observation points using the thin wire approximation, in terms of the local coordinate system defined by $\hat{\ell}$ for the feed, is $R = \sqrt{(\ell - \ell')^2 + a^2}$, which is identical to that given for the straight wire example of Section 2.3.

Since the antenna now consists of at least two different wires, it is also necessary to determine the current at the connection points and the cross terms (or the current from to source points that are on different wires). The connection and cross terms are very similar in their formulations. In fact, the cross terms are really a simplification of the connection terms.

Once again, the starting point for the connection terms is equation (3.19) with different definitions of $\hat{\ell}$ and R. The geometry for a generic connection term and cross term is shown in Fig. 3.3. The connection term consists of four integrals; segments 1 to 3, segments 1 to 4, segments 2 to 3, and segments 2 to 4. The integrals of segments 1 to 3

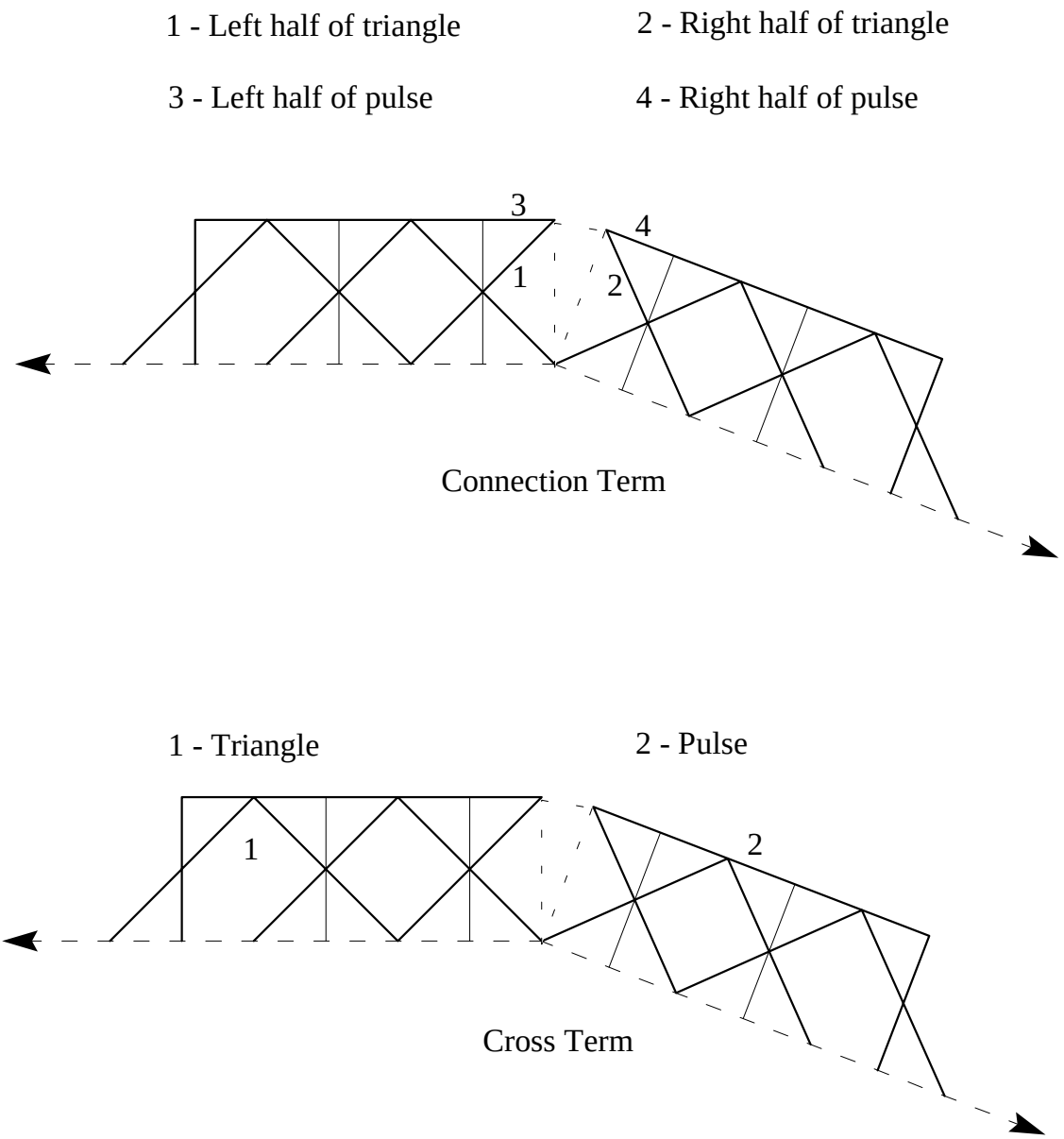

Figure 3.3 Connection and cross term geometry.

and segments 2 to 4 have both segments on the same wire and can be solved using the techniques describe in Section 3.2 and the first part of this section. The remaining two integrals, that is segments 1 to 4 and segments 2 to 3, involve segments on different wires and are described below.

If the source point is on the helix, then its unit vector from (3.20) is

$$\hat{\ell}' = -\hat{x}\cos\alpha\sin\left(\frac{2\pi}{L}\ell'\right) + \hat{y}\cos\alpha\cos\left(\frac{2\pi}{L}\ell'\right) + \hat{z}\sin\alpha \tag{3.20}$$

and its position vector from (3.23) is

$$\vec{r}' = \hat{x}\rho\cos\left(\frac{2\pi}{L}\ell'\right) + \hat{y}\rho\sin\left(\frac{2\pi}{L}\ell'\right) + \hat{z}\left(\ell'\sin\alpha + z_o\right). \tag{3.23}$$

If the observation point is on the straight wire, then its unit vector, $\hat{\ell}$, is the same as defined above in (3.25) and its position vector is given simply by

$$\vec{r} = \hat{x}x + \hat{y}y + \hat{z}z\,. \tag{3.26}$$

The dot product of the unit vectors for the source and observation points is

$$\left(\hat{\ell}\cdot\hat{\ell}'\right) = \frac{-\left(x_2 - x_1\right)\cos\alpha\sin\left(\frac{2\pi}{L}\ell'\right) + \left(y_2 - y_1\right)\cos\alpha\cos\left(\frac{2\pi}{L}\ell'\right) + \left(z_2 - z_1\right)\sin\alpha}{\sqrt{\left(x_2 - x_1\right)^2 + \left(y_2 - y_1\right)^2 + \left(z_2 - z_1\right)^2}} \tag{3.27}$$

and the distance between the source and observation points is approximately

$$R = \sqrt{\left(x - \rho\cos\left(\frac{2\pi}{L}\ell'\right)\right)^2 + \left(y - \rho\sin\left(\frac{2\pi}{L}\ell'\right)\right)^2 + \left(z - \ell'\sin\alpha - z_o\right)^2 + \left(\frac{a + a'}{2}\right)^2}\,. \tag{3.28}$$

The distance, R, is once again based on the thin wire approximation. The radius of the wire used in (3.28) is the average of the radius of the observation point wire, a, and the radius of the source point wire, a'. An alternative to using the average of the two radii is to just use the radius of the source wire, a', signifying that the incident electric field is approximated on the axis of the observation wire. A similar formulation to that shown above can be defined for the complimentary problem of a source point on the straight wire and the observation point on the helix.

The other possible connection term is for the junction of two feed wires. The unit vector for the source point is given by

$$\hat{\ell}' = \frac{\left(x'_2 - x'_1\right)\hat{x} + \left(y'_2 - y'_1\right)\hat{y} + \left(z'_2 - z'_1\right)\hat{z}}{\sqrt{\left(x'_2 - x'_1\right)^2 + \left(y'_2 - y'_1\right)^2 + \left(z'_2 - z'_1\right)^2}} \tag{3.29}$$

and the unit vector for the observation point was given in (3.25). The position vector for the source point is

$$\vec{r}' = \hat{x}x' + \hat{y}y' + \hat{z}z' \tag{3.30}$$

and the position vector for the observation is defined by (3.26). The dot product of the two unit vectors and the approximate distance between the two points is then given by

$$\left(\hat{\ell} \cdot \hat{\ell}'\right) = \frac{\left(x_2 - x_1\right)\left(x'_2 - x'_1\right) + \left(y_2 - y_1\right)\left(y'_2 - y'_1\right) + \left(z_2 - z_1\right)\left(z'_2 - z'_1\right)}{\sqrt{\left(x_2 - x_1\right)^2 + \left(y_2 - y_1\right)^2 + \left(z_2 - z_1\right)^2}\sqrt{\left(x'_2 - x'_1\right)^2 + \left(y'_2 - y'_1\right)^2 + \left(z'_2 - z'_1\right)^2}} \tag{3.31}$$

and

$$R = \sqrt{(x - x')^2 + \left(y - y'\right)^2 + (z - z')^2 + \left(\frac{a + a'}{2}\right)^2} \,. \tag{3.32}$$

The above formulation is for the connection terms between two wires, but is also applicable to the cross terms. The cross terms occur when the entire source point or the entire observation point is on a single wire. In this case, fewer sub-segments are needed. As an example, one segment for the basis function and another segment for the weighting function as shown in Fig. 3.3. The dot product, $\left(\hat{\ell} \cdot \hat{\ell}'\right)$, and the distance between the source and observation points, R, can now be calculated using the same techniques described above for the connection terms. The above theory can also be extended to handle connection points of three or more wires (Miller and Deadrick, 1975).

3.4 Ground Plane Formulation

As stated in Section 3.1, the ground plane is chosen to be in the $x - y$ plane and is perfectly conducting and infinite. The ground plane formulation is based on image theory. The basic concept of image theory is to mirror image the structure and sources above the ground plane across the ground plane and then remove the ground plane. If the current above the ground plane is given by

$$\vec{J} = J_x\hat{x} + J_y\hat{y} + J_z\hat{z} \,, \tag{3.33}$$

then the image current an equal distance below the ground plane is given by

$$\vec{J}_i = -J_x\hat{x} - J_y\hat{y} + J_z\hat{z}\,. \tag{3.34}$$

The image structure still has the same x and y coordinates as the real structure, but the z coordinates for the image structure are the negative of the z coordinates for the real structure. The total electric field at each observation point above the ground plane is now the superposition of the field due to the real current and the field due to the image current. Image theory is only valid for observation points above the ground plane.

In terms of the electric field integral equation of (3.19), only the impedance matrix given by

$$Z_{m,n} = \frac{j}{\omega\varepsilon_o}\left[k^2\int_{\ell_m}\int_{\ell_n}\left(\hat{\ell}\cdot\hat{\ell}'\right)T_n(\ell')G(R)d\ell' d\ell + \left(\int_{\ell_n}\frac{G(R)}{\Delta}\left[P_n^+(\ell') - P_n^-(\ell')\right]d\ell'\right)\Bigg|_{\ell_m^-}^{\ell_m^+}\right], \tag{3.35}$$

is affected by the introduction of image currents to the problem. Eq. (3.35) is extended by adding the integral over the image sources, ℓ_n^i. Thus, the total impedance matrix can be represented by

$$Z_{m,n} = Z_{m,n}^r + Z_{m,n}^i\,, \tag{3.36}$$

where $Z_{m,n}^r$ is due to the real current and $Z_{m,n}^i$ is due to the image current. An example geometry for the ground plane problem via image theory is shown in Fig. 3.4. The formulation will be described in two parts; the connection term at the ground plane and all other terms.

First, consider the ground plane formulation for all the terms except the connection term. The impedance matrix terms due to the image current can be calculated by treating the terms in the same manner as the cross terms described in the previous section. The observation point is still above the ground plane, but the source point is now below the ground plane. As before, (3.19) can be used to solve the problem with new definitions of $\hat{\ell}$ and R.

There are three cases that must be considered when computing the impedance matrix due to the image currents. First, both the source and observation points could be on straight wires. The image of the source point unit vector, $\hat{\ell}'$, is giving by

$$\hat{\ell}'_i = \frac{-\left(x'_2 - x'_1\right)\hat{x} - \left(y'_2 - y'_1\right)\hat{y} + \left(z'_2 - z'_1\right)\hat{z}}{\sqrt{\left(x'_2 - x'_1\right)^2 + \left(y'_2 - y'_1\right)^2 + \left(z'_2 - z'_1\right)^2}} \tag{3.37}$$

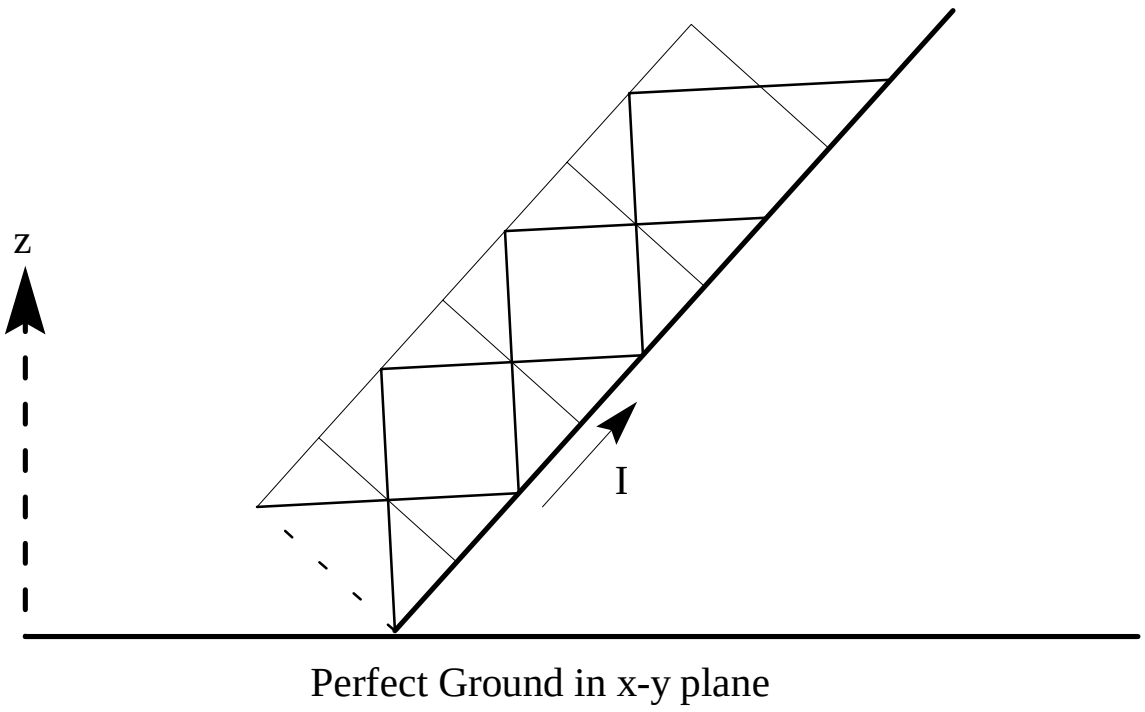

Figure 3.4 Ground plane formulation.
a) Example geometry for ground plane formulation.

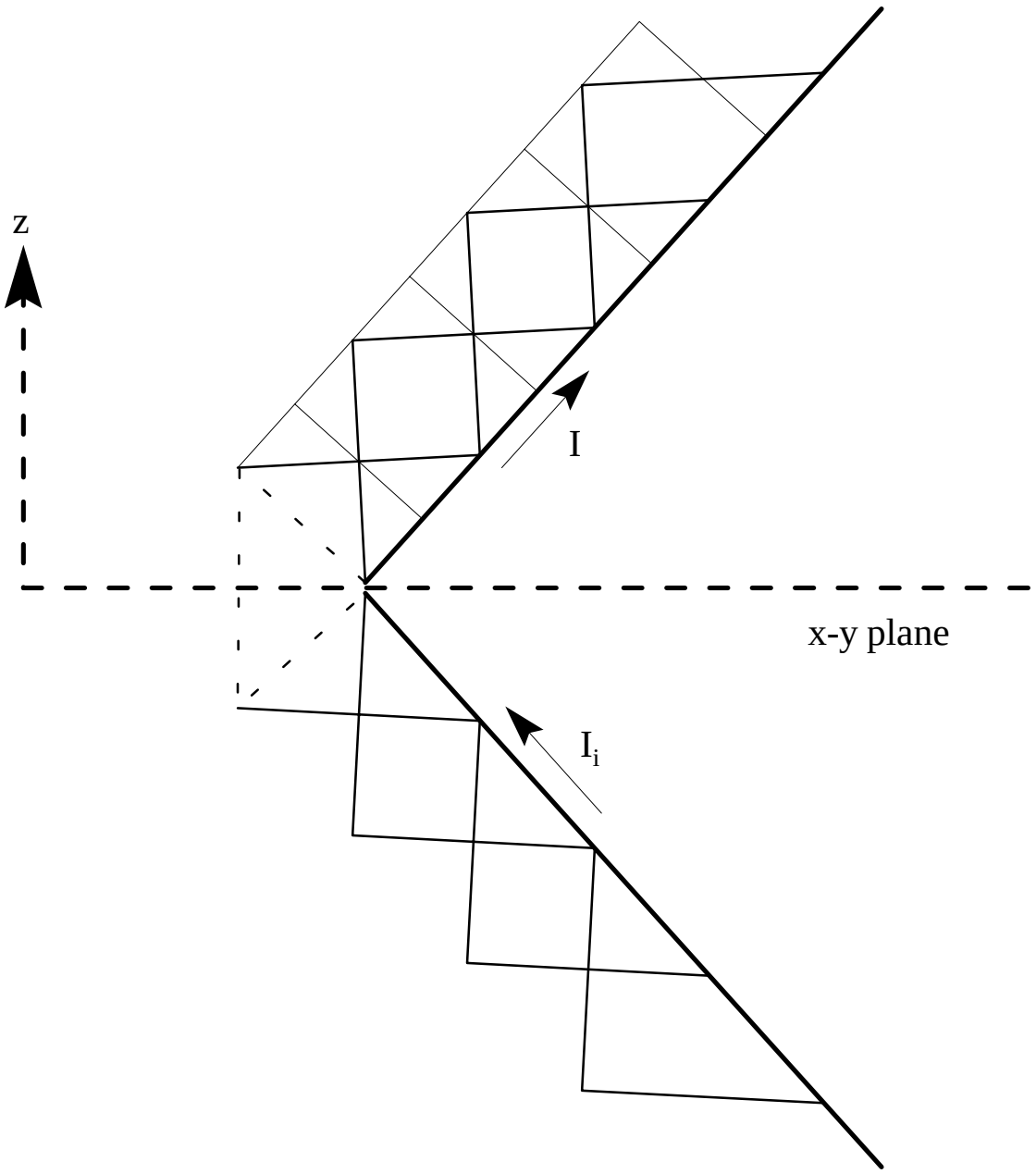

Figure 3.4 Ground plane formulation.
b) Image theory for example ground plane formulation.

and the unit vector for the observation point is still given by (3.25). The dot product, $\left(\hat{\ell}\cdot\hat{\ell}'_i\right)$, can be computed giving

$$\left(\hat{\ell}\cdot\hat{\ell}'_i\right)=\frac{-\left(x_2-x_1\right)\left(x'_2-x'_1\right)-\left(y_2-y_1\right)\left(y'_2-y'_1\right)+\left(z_2-z_1\right)\left(z'_2-z'_1\right)}{\sqrt{\left(x_2-x_1\right)^2+\left(y_2-y_1\right)^2+\left(z_2-z_1\right)^2}\sqrt{\left(x'_2-x'_1\right)^2+\left(y'_2-y'_1\right)^2+\left(z'_2-z'_1\right)^2}}. \quad (3.38)$$

The distance between the source image and observation points is found by negating the z coordinate of the source point in (3.32) giving

$$R=\sqrt{(x-x')^2+\left(y-y'\right)^2+(z+z')^2+\left(\frac{a+a'}{2}\right)^2}\,. \quad (3.39)$$

The other two cases can be found by using the same procedure as described above. If the source point is on the helix image and the observation point is on a feed wire or vice versa, the dot product, $\left(\hat{\ell}\cdot\hat{\ell}'_i\right)$, is given by

$$\left(\hat{\ell}\cdot\hat{\ell}'_i\right)=\frac{\left(x_2-x_1\right)\cos\alpha\sin\left(\frac{2\pi}{L}\ell'\right)-\left(y_2-y_1\right)\cos\alpha\cos\left(\frac{2\pi}{L}\ell'\right)+\left(z_2-z_1\right)\sin\alpha}{\sqrt{\left(x_2-x_1\right)^2+\left(y_2-y_1\right)^2+\left(z_2-z_1\right)^2}}, \quad (3.40)$$

and the distance between the two points is approximated by

$$R=\sqrt{\left(x-\rho\cos\left(\frac{2\pi}{L}\ell'\right)\right)^2+\left(y-\rho\sin\left(\frac{2\pi}{L}\ell'\right)\right)^2+\left(z+\ell'\sin\alpha+z_o\right)^2+\left(\frac{a+a'}{2}\right)^2}\,. \quad (3.41)$$

The final case is when both the source image and observation points are on the helix. The dot product, $\left(\hat{\ell}\cdot\hat{\ell}'_i\right)$, and the distance, R, for this case are given by

$$\left(\hat{\ell}\cdot\hat{\ell}'_i\right)=-\cos^2\alpha\cos\left(\frac{2\pi}{L}(\ell-\ell')\right)+\sin^2\alpha \quad (3.42)$$

and

$$R=\sqrt{\left(\frac{L\cos\alpha}{\pi}\right)^2\sin^2\left(\frac{\pi}{L}(\ell-\ell')\right)+\left((\ell+\ell')\sin\alpha+2z_o\right)^2+a^2}\,. \quad (3.43)$$

The connection term at the ground plane will be treated differently than the other terms described above. The ground connection term consists of one row and one column

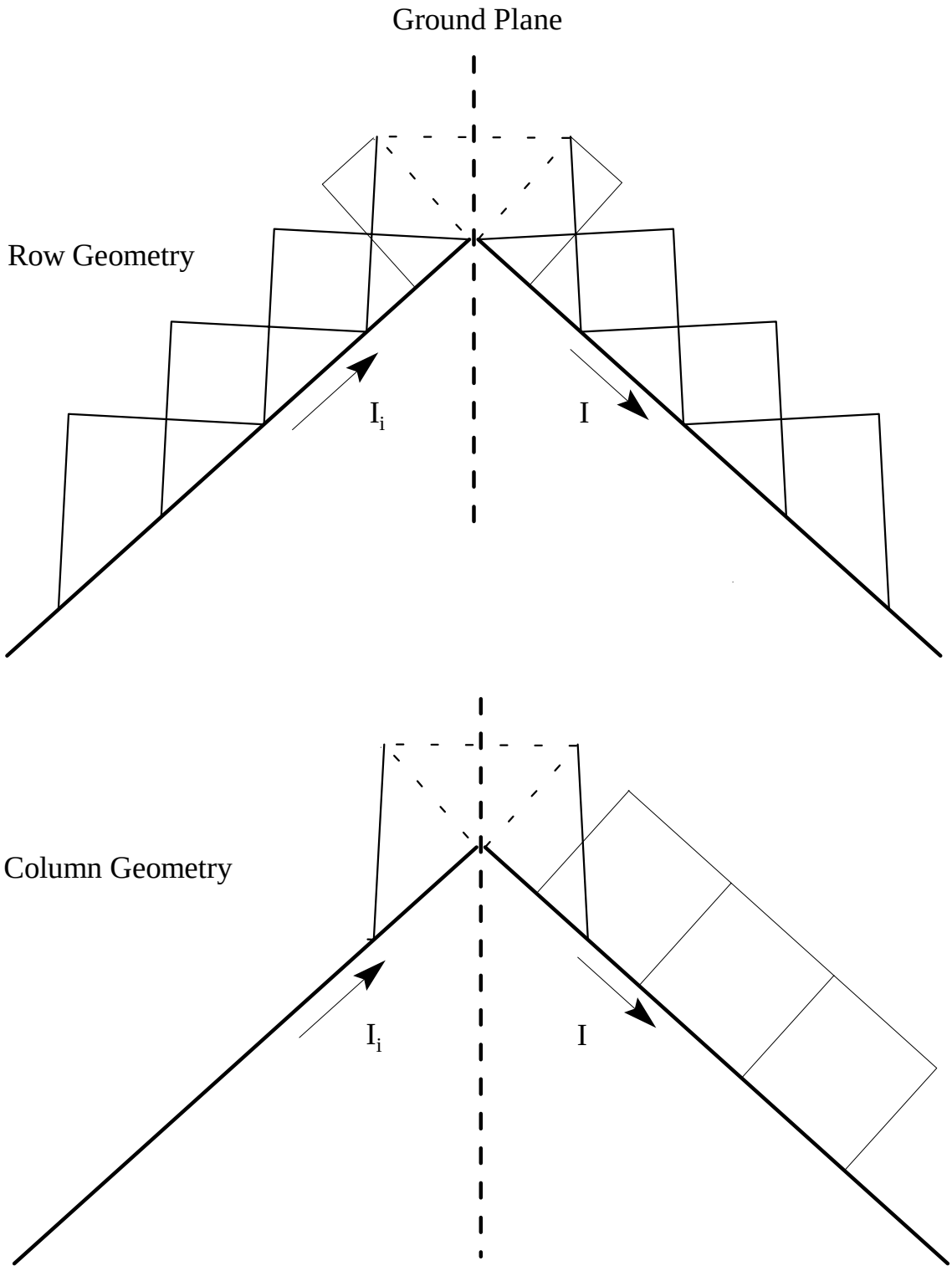

Figure 3.5 Geometry for the row and column of the ground plane connection.

in the impedance matrix. Fig. 3.5 shows the geometry for the row and column of the impedance matrix corresponding to the ground plane connection. The formulation is easier to understand if the pulse weighting function at the ground connection is treated as a full width pulse centered about the ground plane, rather than the half width pulse of Fig. 3.4. From the symmetry of the problem it can be seen that the contributions of the real current at the left half of the pulse are equal to the contributions of the image currents at the right half of the pulse. Also, the contributions of the image currents at the left half of pulse are equal to the contributions of the real currents at the right half of the pulse. Using this symmetry, the row of the impedance matrix corresponding to the ground plane connection can be found by doubling the contributions of the real currents at the right half of the pulse. The column corresponding to the ground plane connection is calculated using the same procedure as described for the general ground plane term, except the image current is described by half a triangular basis function as shown in Fig. 3.5. The ground plane also effects the voltage source if it is applied at the unknown which spans the ground plane. The image of the voltage source adds to the real source causing the total voltage to double. The theory and concepts described in this chapter will be demonstrated and validated in the following chapter with some simple antenna problems.

4. Normal Mode Helix

In the previous chapter, we presented the theory used in the development of the Moment Method code for the solution of the currents on a helix antenna. In this chapter, the code will be validated and compared to other codes using the normal mode helix as an example. First, a normal mode helix is used to approximate a straight wire antenna, which is then compared to the straight wire example discussed in Chapter 2. Then, as an extension of approximating a straight wire with a helix, a comparison between a dipole and a normal mode helix will be presented. Finally, the convergence characteristics of the Curved code for a normal mode helix will be compared to the Numerical Electromagnetics Code (NEC) (Burke, 1992), and MININEC (Rockway and Logan, 1995). This will provide a validation of the code and show the advantage of using curved basis and testing functions over straight segments.

4.1 Straight Wire Approximation

A helix antenna reduces to a straight wire structure when the pitch angle, α, equals 90°. The code must check for a pitch angle of exactly 90° because the calculation of the length of one turn of the helix blows up, since $L = \frac{2\pi\rho}{\cos\alpha}$. The code has been modified to accommodate a pitch angle of 90°, but it is not really necessary since a pitch angle of 89° approximates a straight wire quite well. Also, since the pitch angle is not exactly 90°, all of the code pertaining to the helix will be executed, providing an excellent check of the code.

For comparison a helix with $\alpha = 89°$ will be compared to the straight wire example of Section 2.3. The example is for a dipole antenna with a length of 0.47λ and a wire diameter of 0.005λ. The parameters of the helix approximating the straight wire are given in Table 4.1. Note that the number of turns is very small since only a portion of a turn is needed to create the necessary dipole length. Both antennas are broken into 6 segments. The currents on the half wave dipole obtained in Section 2.3 and using the helix approximation are

$$I_{Straight} = 10^{-3}\begin{bmatrix} 8.1\angle -1.0° \\ 13.0\angle 1.9° \\ 14.8\angle 7.5° \\ 13.0\angle 1.9° \\ 8.1\angle -1.0° \end{bmatrix} \text{ and } I_{Helix} = 10^{-3}\begin{bmatrix} 8.0\angle -2.8° \\ 12.9\angle 0.1° \\ 14.7\angle 5.8° \\ 12.9\angle 0.1° \\ 8.0\angle -2.8° \end{bmatrix}.$$

The input impedance from Section 2.3 is $66.9 - j8.8$ ohms and the input impedance using the helix approximation is $67.7 - j6.9$ ohms. For 12 segments, the input impedance from

Section 2.3 is $71.3 - j1.8$ ohms versus $73.8 + j2.3$ ohms. The data shows that the straight wire example and the helix approximation converge at different rates, but in general the helix approximation compares very well for both current and input impedance. A pitch angle of exactly 90° gives the same results as the 89° approximation for the number of significant digits shown. This means that the small differences in the current and input impedance shown above are due to the use of a sinusoidal basis function for the straight wire and a triangular basis function for the helix.

Table 4.1 Parameters for Helix Approximation to Straight Wire Antenna

Helix Parameter	Numerical Values
Helix Radius, ρ	0.02λ
Pitch Angle, α	89°
Number of Turns, N	0.06527
Wire Radius, a	0.005λ

Another useful example is that of a quarter-wave monopole with a perfect ground plane. This example checks that the code can handle the ground plane properly for both computing the currents and for imaging the voltage source, which is applied at the connection of the monopole and the ground. The same helix approximation to a straight wire that was used above will also be used for the monopole example. The only change in the helix parameters is to reduce the number turns, N, by one-half giving $N = 0.032635$. The resulting current solution for 6 segments is

$$I_{Monopole} = 10^{-3}\begin{bmatrix} 28.1\angle 0.6° \\ 27.3\angle -3.9° \\ 25.0\angle -6.0° \\ 21.1\angle -7.7° \\ 15.8\angle -9.1° \\ 9.3\angle -10.4° \end{bmatrix}.$$

and the input impedance is $35.6 - j0.3$ ohms. Not that row 1 of the current vector represents the unknown located at the ground plane. As expected the peak current of 28.1 mA for the monopole is about twice the peak current for the dipole, and the input impedance of the monopole is approximately half that of the dipole example shown above.

4.2 Dipole vs. Normal Mode Helix

In the previous section, a normal mode helix was used to approximate a straight wire as a check of the Curved code versus standard dipole results. It may also be interesting to compare a normal mode helix with a total wire length of 0.5λ to a straight dipole antenna of the same length. Fig. 4.1 shows the current along a 0.5λ dipole with $a = 0.001\lambda$ and a normal mode helix with parameters: $\rho = 0.0273\lambda$, $\alpha = 12°$, $N = 2.851$ turns, $a = 0.001\lambda$, and 50 segments. Both the helix current and the dipole current are sinusoidal in shape, but the helix current is about 3 times greater in magnitude at the center of the antenna due to coupling effects when the wire is wound into a helix. Also, the shape of the current plots implies the two antennas have slightly different input impedances. The dipole current dips slightly at its center signifying an inductive impedance, whereas the helix current peaks at its center implying a capacitive impedance. The actual values of the input impedance for the dipole and helix are $84.8 + j43.6\Omega$ and $3.9 - j34.6\Omega$, respectively.

Given the similarities between the dipole and normal mode helix in terms of the wire structure and basic sinusoidal current shape, it should be possible to simulate a normal mode helix as a straight wire with inductive loading. As an example, consider a center fed normal mode helix in free space with the following parameters: $\rho = 0.007\lambda$, $\alpha = 15°$, $N = 17$ turns, $a = 0.0007\lambda$, and 340 segments. The helix has a height of 0.2λ, a total wire length of 0.774λ, and an input impedance of $14.4 - j4.5\Omega$. The normal mode helix described above can be simulated by inductively loading a dipole where the length of the dipole equals the height of the helix. Specifically, the dipole has a length of 0.2λ, a wire radius of $a = 0.007\lambda$, which equals the radius of the helix, and the dipole is broken into 10 segments. The following data was computed using the WIRE antenna code (Davis, 1995).

Without loading, the input impedance of the dipole is $6.7 - j270.1\Omega$, but when loaded with a reactance of $j68.6\Omega$ at each unknown the input impedance becomes $14.1 - j4.6\Omega$, which compares very well with the input impedance of the normal mode helix. As a check of the loading process, if the dipole is broken into 20 segments and again uniformly loaded, half the reactance of the 10 segment example should be required to match the dipole with the helix. And as expected, a uniform load of $j33.6\Omega$ for the 20 segment case results in an input impedance of $14.6 - j4.3\Omega$ for the dipole. An approximate number for the reactance can be computed from simple theory by using the formula for the inductance of a solenoid (Edminister, 1993),

$$L = \frac{\mu_o N^2 A}{\ell}, \tag{4.1}$$

where N is the number of turns, A is the cross-sectional area, and ℓ is the axial length of the solenoid. For the 20 segment dipole case: $A = 0.000154\lambda^2$, $N = 0.85$ turns, and

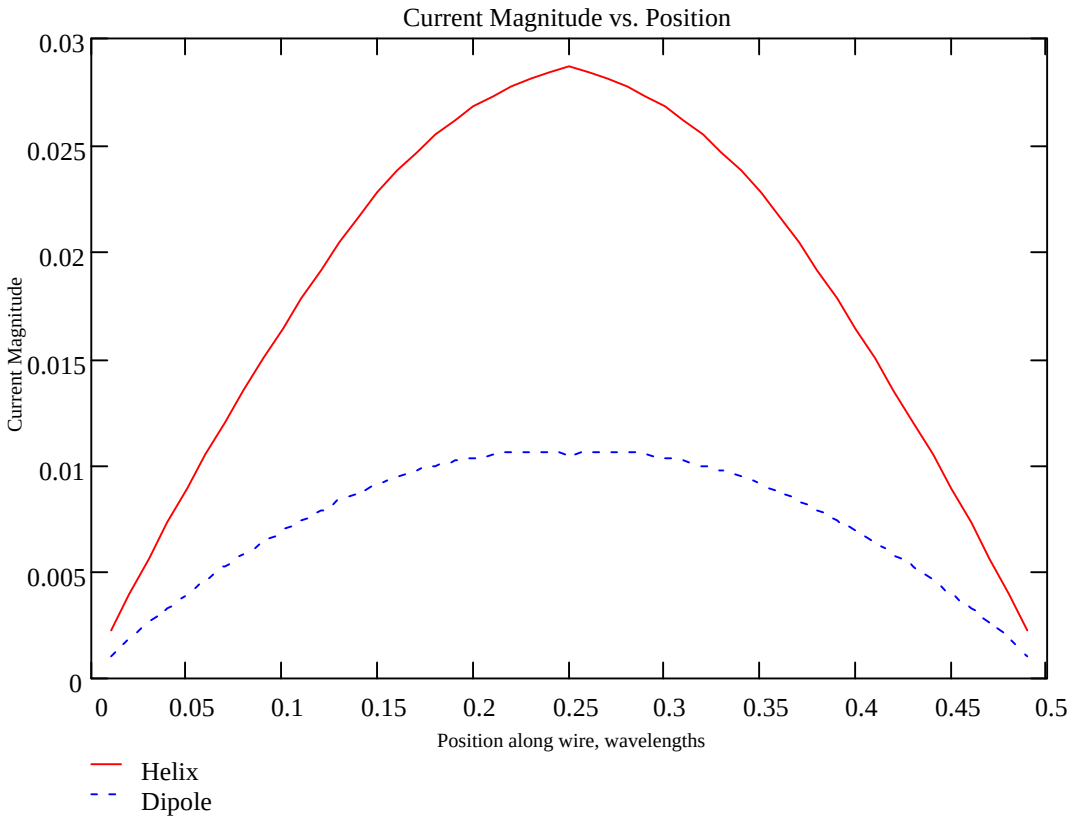

Figure 4.1 Current magnitude vs. position along antenna for a dipole and a normal mode helix. Both antennas have a wire length of 0.5λ.

$\ell = 0.01\lambda$ for one segment. From (4.1) the theoretical inductance is computed and the corresponding reactance per dipole segment is $j26.4\Omega$. The simple theory matches fairly well with the reactance found using WIRE given that the theory is for a distributed inductance but WIRE uses lumped loads at each unknown. Also, the appropriateness of (4.1) may be questionable since the formula is for solenoids of small cross-sectional area and many turns. In practice, inductive loading may be desirable when modeling antennas such as a helix wound out of a spring, where the spring can be simulated by inductively loading the helix.

4.3 Validation and Convergence Comparison to NEC and MININEC

The convergence characteristics of the Curved code are shown to validate the results of the code and to demonstrate the advantage of using curved basis and testing functions. Consider a center fed normal mode helix in free space with parameters as given in Fig 4.2. The convergence plots of Fig. 4.3 show that significantly less unknowns are needed when using the Curved code versus the conventional straight wire approximation used in NEC and MININEC. For the example of Fig. 4.3, both NEC and MININEC are fairly well converged at approximately 400 segments, or 40 segments per turn, and the Curved code is fairly well converged at 50 segments, or 5 segments per turn. This corresponds to an improvement of about 8:1 when using the Curved code. It is also useful to check the convergence properties of the admittance as shown in Fig. 4.4. The admittance convergence properties are similar to those of the impedance. The Curved code performs well at about 15 to 20 segments per turn, but NEC and MININEC are still questionable at 50 segments per turn.

A quantitative way of comparing the three codes is to compute the percent convergence error for the impedance convergence plots. For each code, its percent error is calculated relative to its impedance value at 500 segments as follows,

$$\%Error = \frac{\left|Z - Z_{500}\right|}{Z_{500}} \times 100 \,. \tag{4.2}$$

The percent error of the three codes is shown in Fig. 4.5. The numerical value of the error is not as important as the relative error between the codes. For example, at 100 segments the Curved code has 20 times less percent error than MININEC and about 30 times less than NEC.

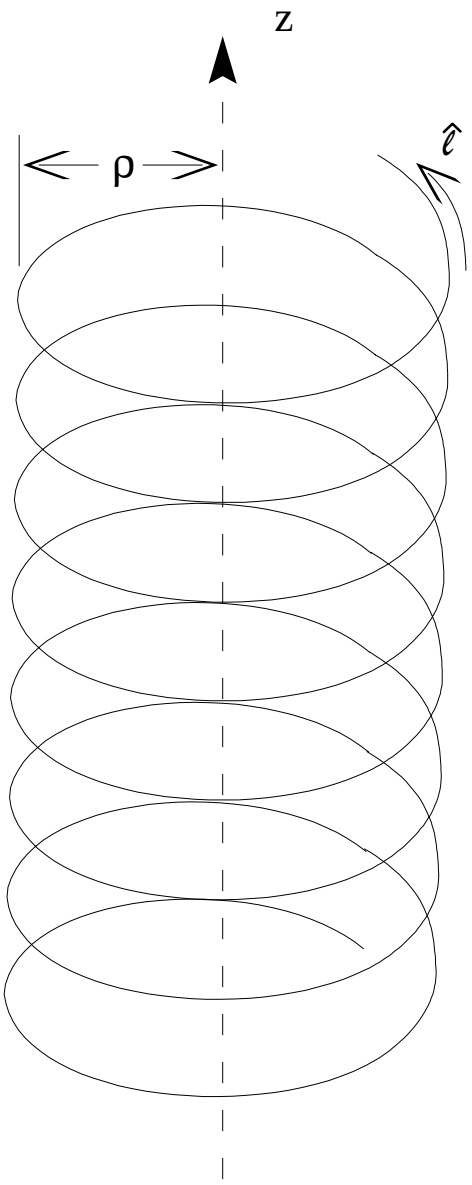

Parameters: $\rho = 0.0273\lambda$
$\alpha = 12°$
$N = 10$ turns
$a = 0.001\lambda$
Center Fed

Figure 4.2 Normal mode helix geometry and parameters.

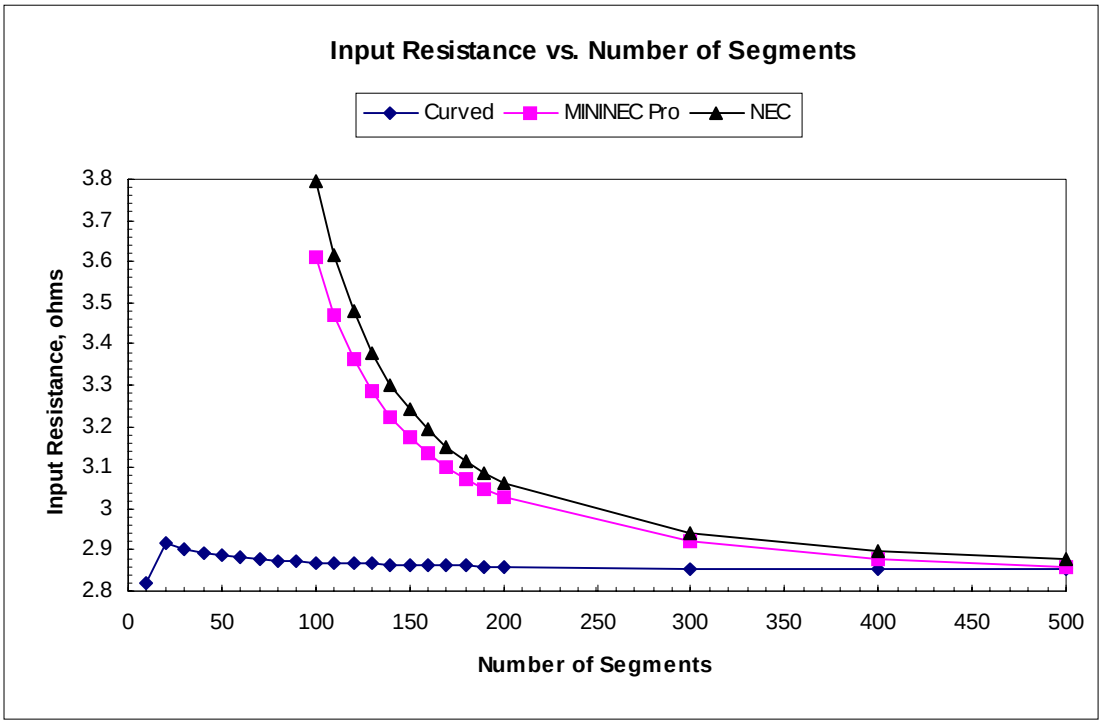

(a) Input resistance.

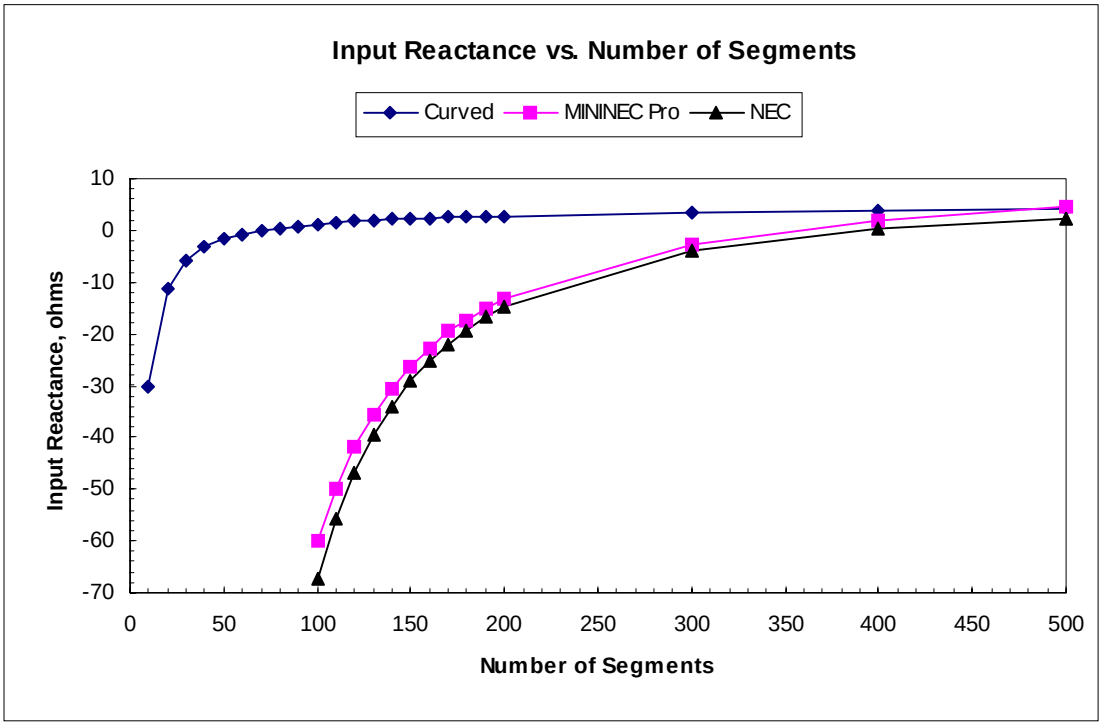

(b) Input reactance.

Figure 4.3 Normal mode helix impedance convergence plots.
Helix parameters: $\rho = 0.0273\lambda$, $\alpha = 12°$, $N = 10$ turns, $a = 0.001\lambda$, Center Fed

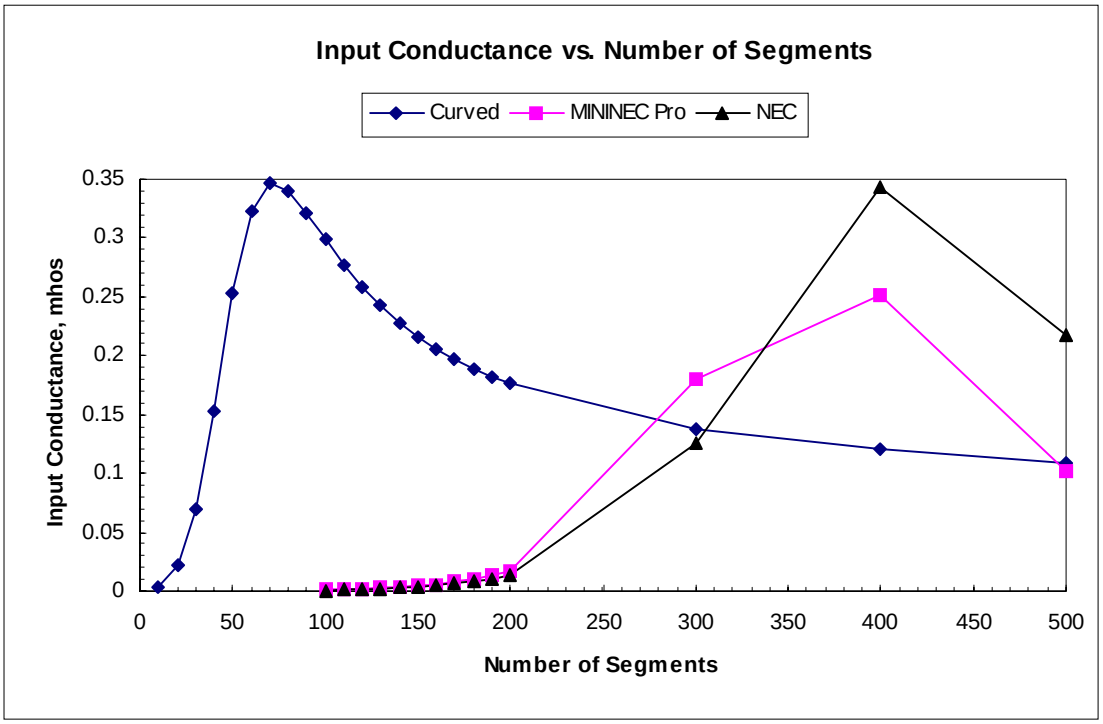

(a) Input conductance.

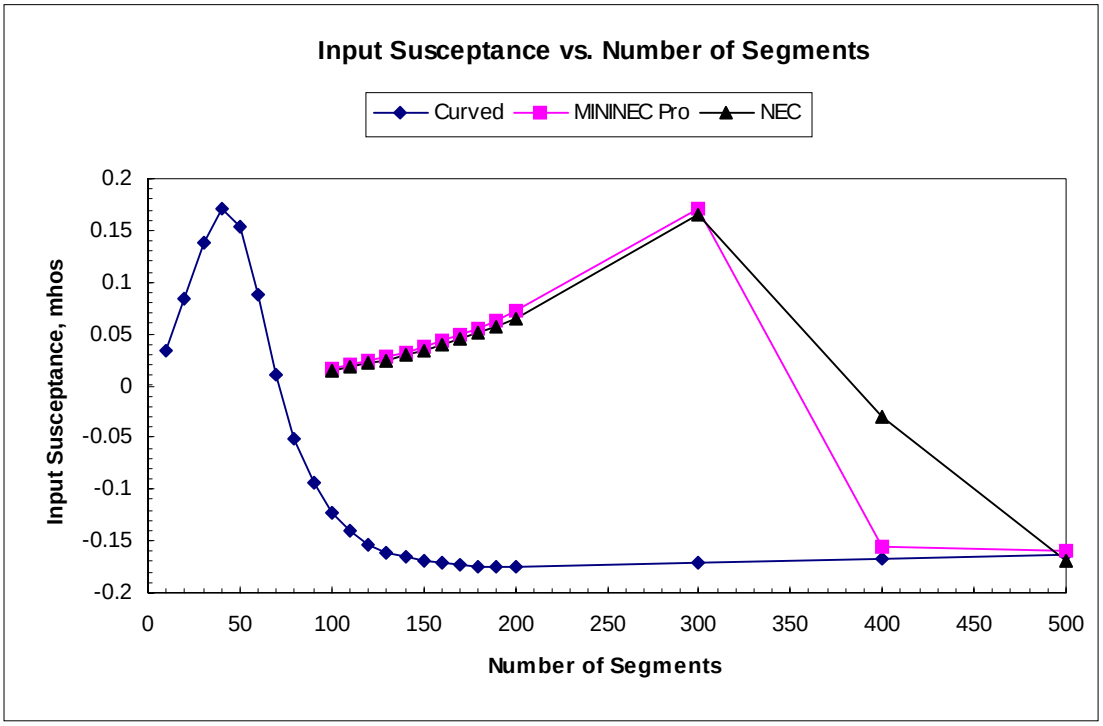

(b) Input susceptance.

Figure 4.4 Normal mode helix admittance convergence plots.
Helix parameters: $\rho = 0.0273\lambda$, $\alpha = 12°$, $N = 10$ turns, $a = 0.001\lambda$, Center Fed

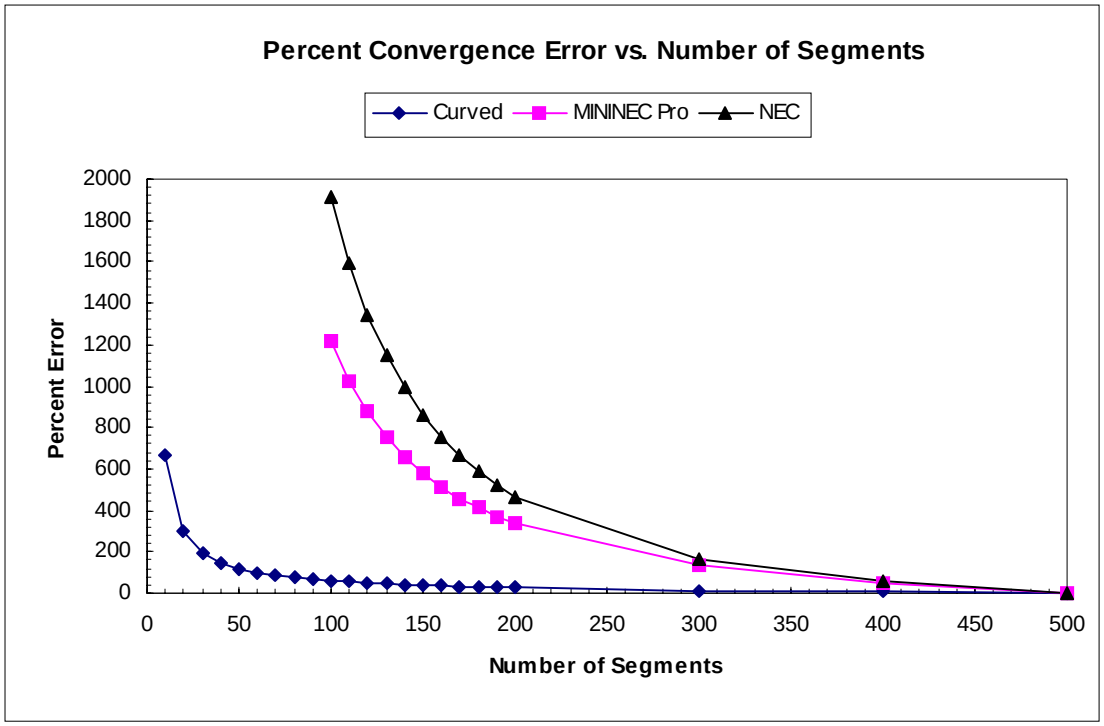

Figure 4.5 Percent error of normal mode helix convergence plots.
Helix parameters: $\rho = 0.0273\lambda$, $\alpha = 12°$, $N = 10$ turns, $a = 0.001\lambda$, Center Fed

4.4 Conclusions

In this chapter, it has been shown that the Curved code outperforms NEC and MININEC in all areas that were considered, that is impedance and admittance convergence and percent error. The use of curved segments allows a more accurate modeling of the geometry of a normal mode helix than the straight wire approximation used in NEC and MININEC. This allows the Curved code to accurately model the helix with approximately 8 times fewer unknowns than the other codes. It has also been shown that an inductively loaded dipole can be used to simulate a normal mode helix. It is believed that the accuracy of predicting the necessary load impedance from theory would increase for more tightly wound helices. The next chapter will investigate the convergence properties of the axial mode helix along with some interesting feed effects.

5. Axial Mode Helix

The major differences between a normal mode helix and an axial mode helix is the radius of the helix with respect to wavelength and the presence of the a ground plane. The radius of a normal mode helix is much smaller than a wavelength which results in a radiation pattern normal to the axis of the helix. The axial mode helix has a radius corresponding to a circumference for one turn of approximately $\frac{3}{4}\lambda < C < \frac{4}{3}\lambda$ (Stutzman and Thiele, 1998), which gives rise to radiation pattern maxima along the axis of the helix. The axial mode helix is usually backed by a ground plane to cut off one of the lobes of the pattern to create a pencil beam forward radiation pattern. In this chapter, the convergence properties of the axial mode helix will be investigated in terms of its impedance and radiation pattern. Bandwidth and feed effects for two different feed structures will also be examined.

5.1 Axial Mode Helix in Free Space

As stated previously, the axial mode helix is usually backed by a ground plane. However, for comparison to the normal mode helix presented in the last chapter, a center fed axial mode helix in free space will initially be considered. The geometry and parameters for the 20 turn helix are shown in Fig. 5.1. The helix radius is chosen such that the circumference of one turn equals a wavelength at mid-band. The impedance and admittance convergence properties for this helix are shown in Fig. 5.2 and Fig. 5.3, respectively. From the figures, it is apparent that the Curved code does not give as much an improvement over NEC and MININEC for the axial mode helix as it does for the normal mode helix. The improvement in convergence ranges from a high of about 4:1 for the reactance down to approximately 2:1 for the susceptance. In terms of segments per turn, the Curved code works well for 5 to 10 segments per turn while the other codes required 20 segments per turn. Notice that NEC and MININEC converge at about 400 segments (20 segments per turn) for all four plots, but the convergence of the Curved code varies slightly, between 100 and 200 segments (5 to 10 segments per turn) for the four plots.

The difference in the improvement for the axial mode helix compared to the normal mode helix is due to the current distribution on the antenna. The current distribution for the 20 turn axial mode helix in free space is shown in Fig. 5.4. For the normal mode helix the current is approximately uniform over one turn so the determining factor is how well the code models the geometry of the antenna. But for the axial mode helix, one turn is about equal to a wavelength. The accuracy with which the code models the current distribution on the antenna is now the most important criteria. How well the code models the curve of the helix is now a secondary consideration, which results in a much smaller improvement in the number of segments for the Curved code compared to NEC and MININEC.

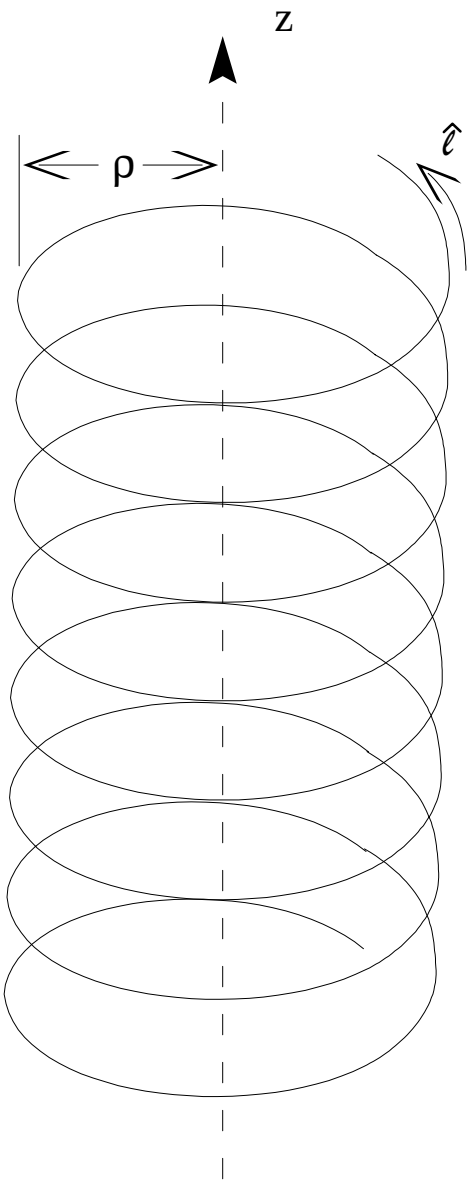

Parameters: $\rho = 0.159\lambda$
$\alpha = 13°$
$N = 20$ turns
$a = 0.001\lambda$
Center Fed

Figure 5.1 Axial mode helix geometry and parameters.

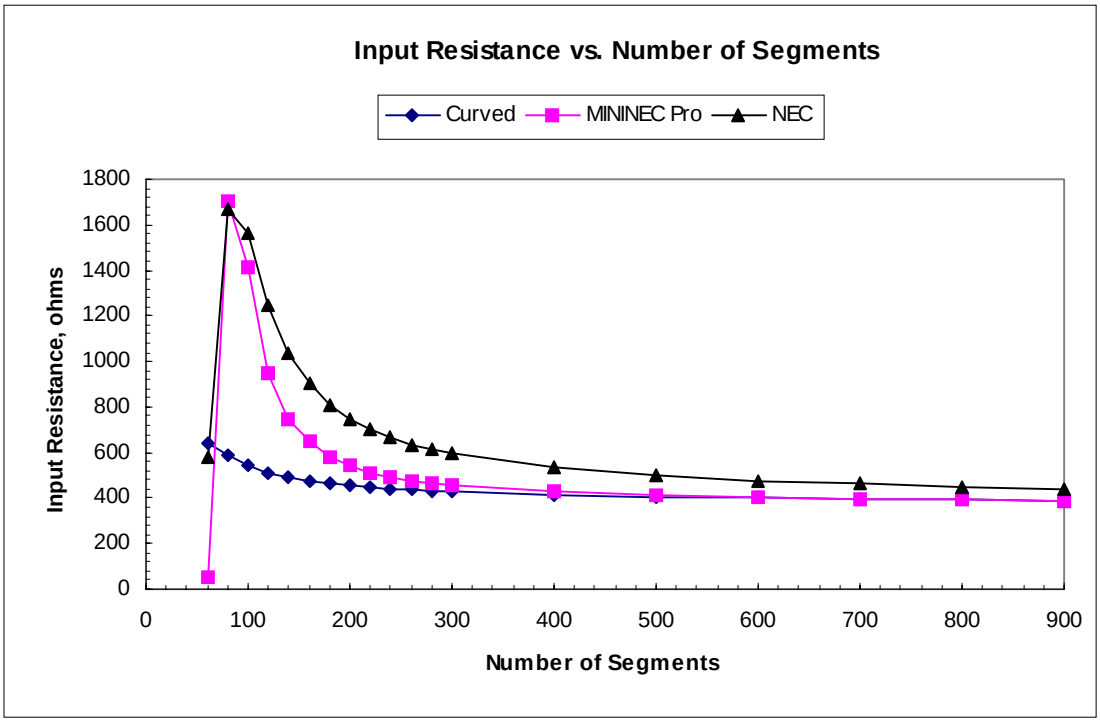

(a) Input resistance.

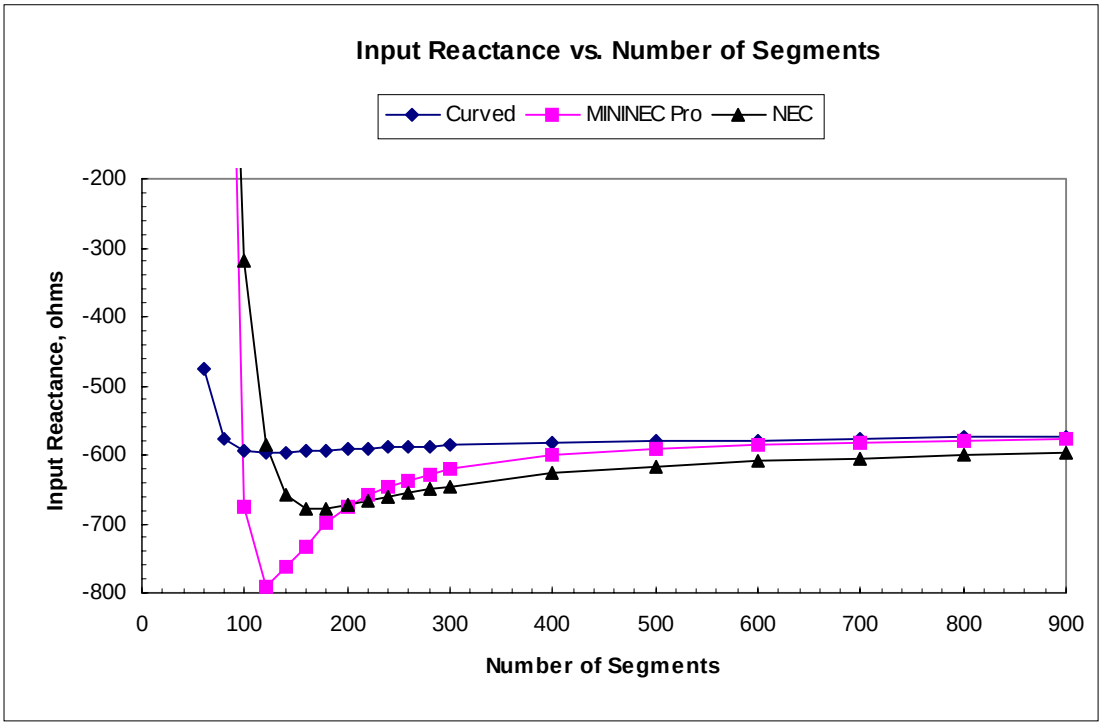

(b) Input reactance.

Figure 5.2 Axial mode helix in free space impedance convergence plots. Helix parameters: $\rho = 0.159\lambda$, $\alpha = 13°$, $N = 20$ turns, $a = 0.001\lambda$, Center Fed

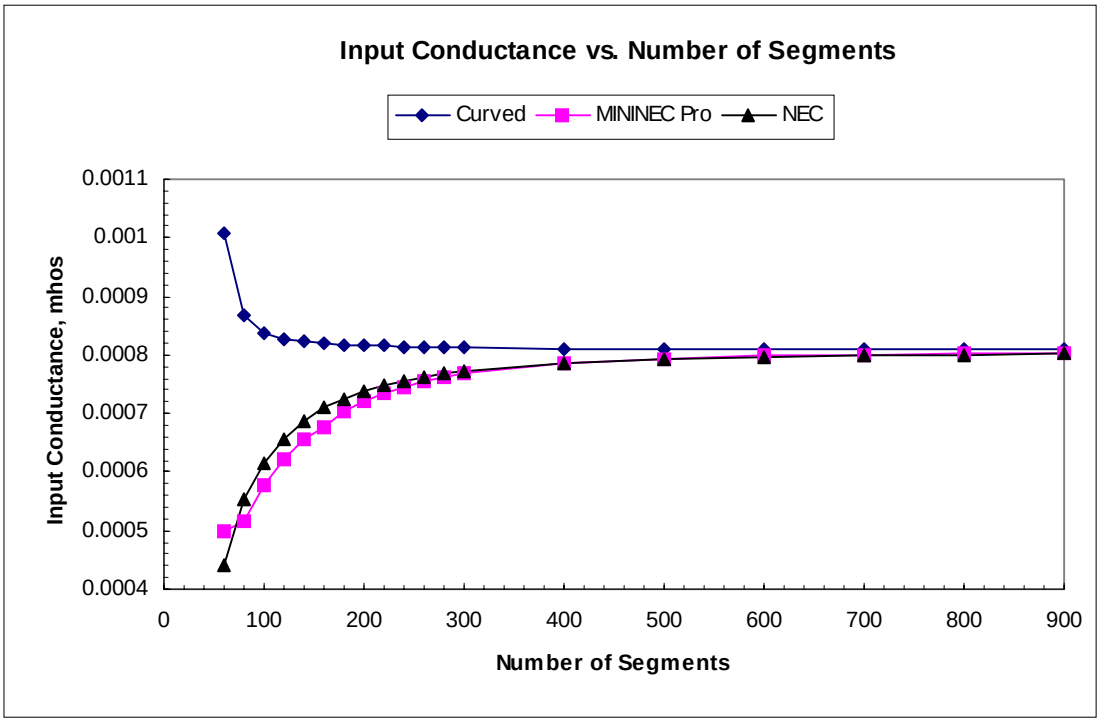

(a) Input conductance.

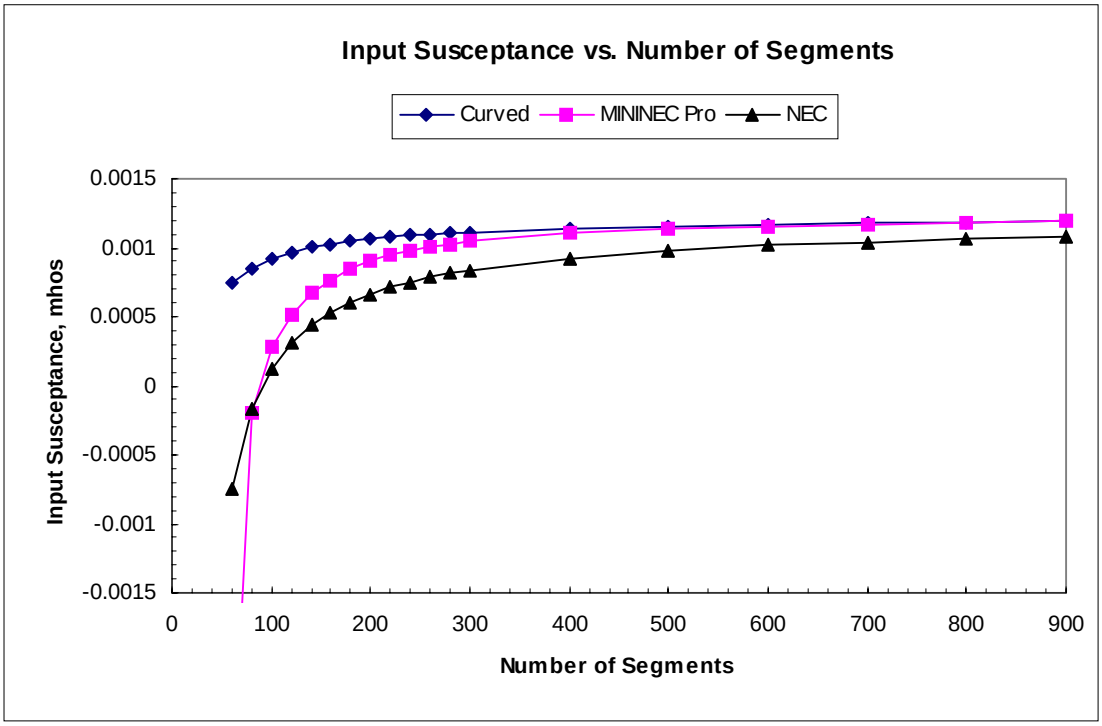

(b) Input susceptance.

Figure 5.3 Axial mode helix in free space admittance convergence plots. Helix parameters: $\rho = 0.159\lambda$, $\alpha = 13°$, $N = 20$ turns, $a = 0.001\lambda$, Center Fed

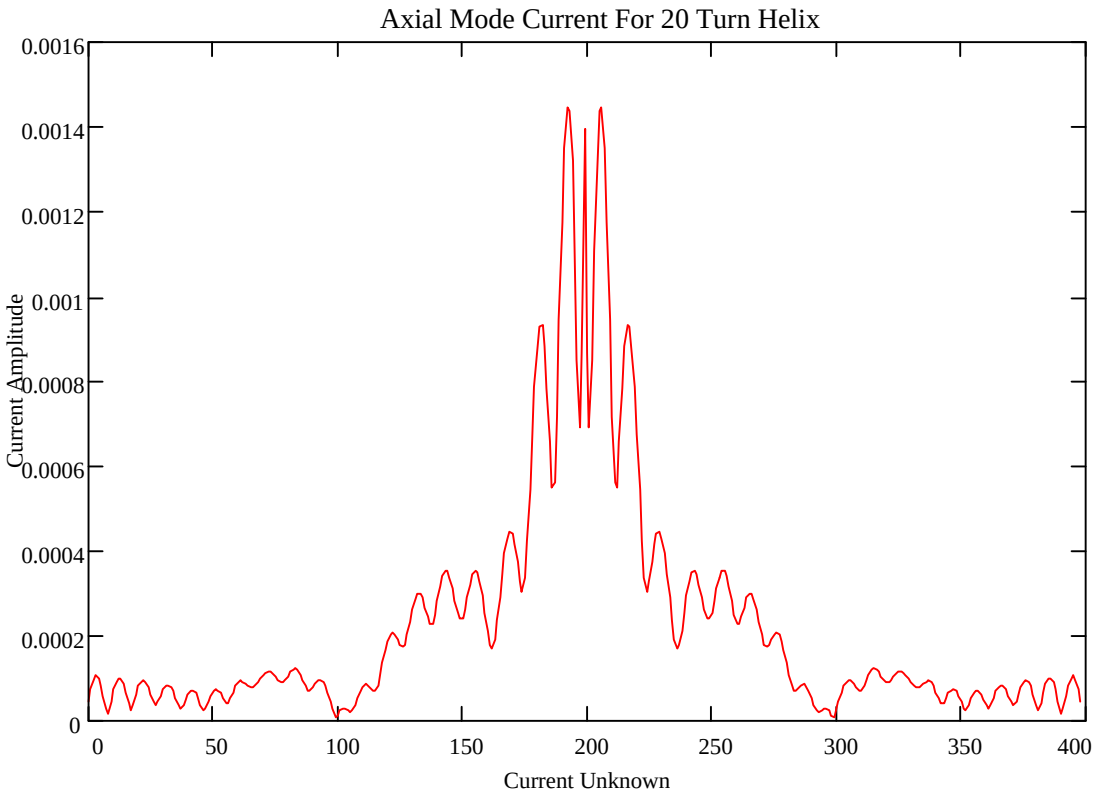

Figure 5.4 Axial mode helix in free space current distribution. The values on the horizontal axis represent the number of the current expansion function, but the plot is more easily understood it the horizontal axis is taken to be position along the helix.

Helix parameters: $\rho = 0.159\lambda$, $\alpha = 13°$, $N = 20$ turns, $a = 0.001\lambda$, Center Fed

5.2 Axial Mode Helix Over Ground

The axial mode helix in free space was presented in the previous section to demonstrate the effect of the current distribution versus approximating the geometry of the helix. The effects of an infinite PEC ground plane and a small feed wire on the convergence characteristics for an axial mode helix will be considered in this section. The feed wire is a small straight wire segment from the end of the helix down to the ground plane as shown in Fig. 5.5. The feed wire is broken into 2 segments with the voltage source located at its center.

The impedance convergence plots for the axial mode helix over ground are shown in Fig. 5.6. Convergence is not shown for NEC because it is unable to model the antenna in the same manner as the Curved code and MININEC. The Curved code is much smoother than MININEC, but both codes converge at about 200 segments. The lack of improvement for convergence of the Curved code versus MININEC is probably due to the feed being located on the straight feed wire. Neither the size nor shape of the feed region varies as the number of unknowns on the helix is increased. Because of the stability of the feed region, the advantages of the Curved code demonstrated in previous examples do not come into effect.

Even though the Curved code does not show improvement in impedance convergence, an improvement in pattern convergence was investigated. Since the pattern is dominated by the current on the helix, not the current on the small feed wire, the Curved code should out perform MININEC because it can more accurately model the current on the helix for a fewer number of unknowns. The patterns for the helix of Fig. 5.5 are shown in Fig 5.7 and Fig. 5.8 for the helix with 50, 100, and 200 segments. Fig. 5.7 shows the theta-component of the electric field versus theta and Fig. 5.8 shows the phi-component of the electric field versus theta, where theta and phi are standard spherical coordinates. Both Fig. 5.7 and Fig. 5.8 are theta cuts for phi equal zero, and the plots are normalized to the 200 segment curve. The feed wire is located in the $\phi = 0°$ plane. The pattern plots show a significant improvement in pattern performance for the Curved code. Pattern performance refers to the general pattern shape including side lobe and null formation as well as peak pattern values. The 200 segment patterns from MININEC and the Curved code match well as expected for this 10 turn helix, since Sec. 5.1 has shown that MININEC adequately converges at about 20 segments per turn. However, the Curved code yields much better patterns for 50 and 100 segments than MININEC.

Another important parameter is the axial ratio, which is a measure of the polarization ellipse. A perfect dipole would have an axial ratio of infinity and a infinite helix would have pure circular polarization on axis, or an axial ratio of one. For the axial mode helix considered in this section, the axial ratio should be close to one at theta equals zero and increase as theta increases. Using the techniques outlined in Stutzman (1993) the axial ratio was computed for the helix of Fig. 5.5 with 50, 100, and 200 segments, and the results are shown in Fig. 5.9. Once again, the Curved code shows faster convergence

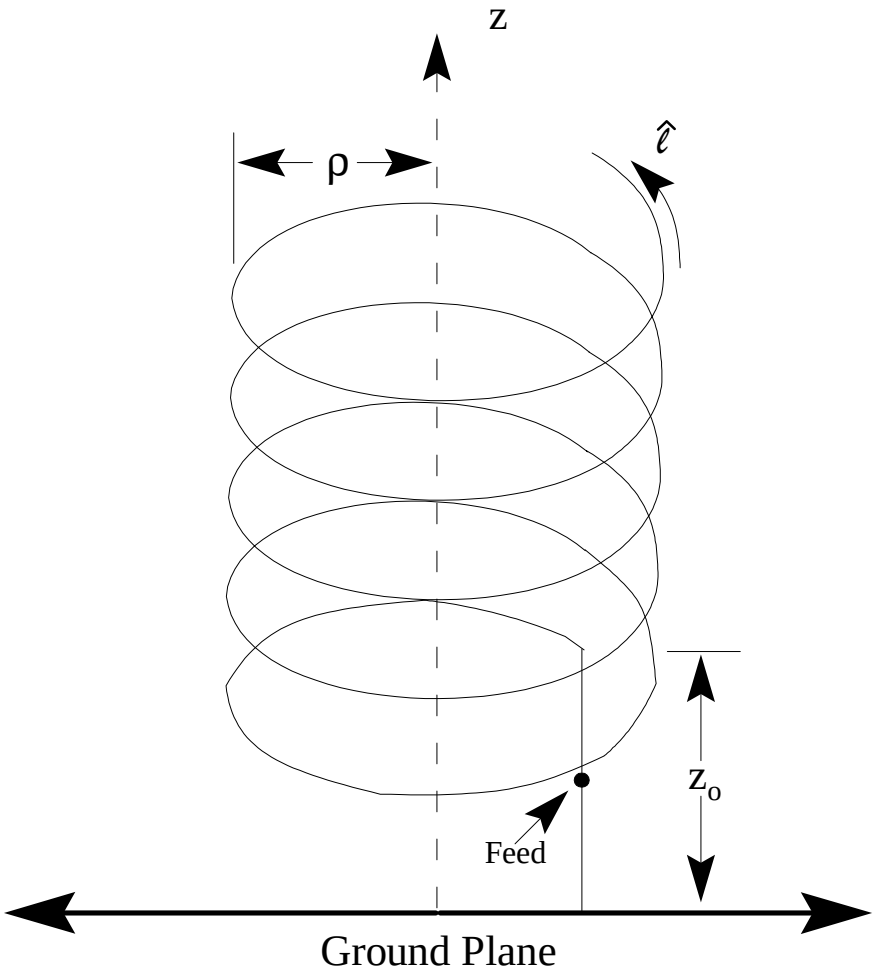

Parameters: $\rho = 0.159\lambda$
$\alpha = 13°$
$N = 10$ turns
$z_o = 0.1\lambda$
$a = 0.001\lambda$

Figure 5.5 Axial mode helix over ground geometry and parameters.

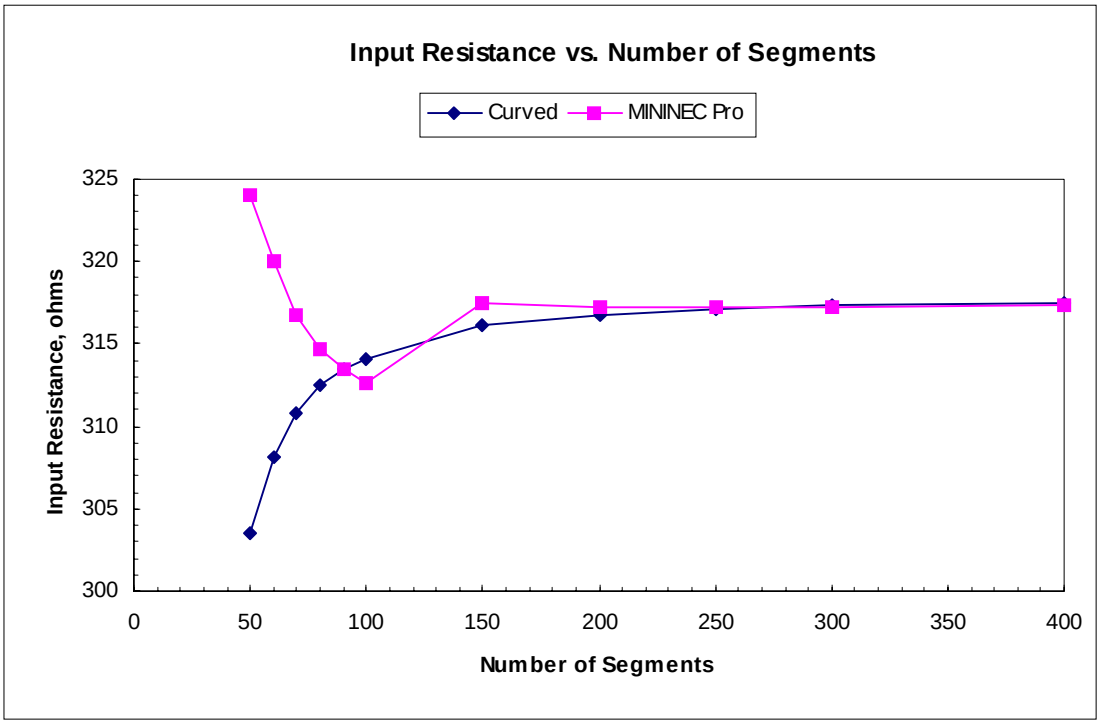

(a) Input resistance.

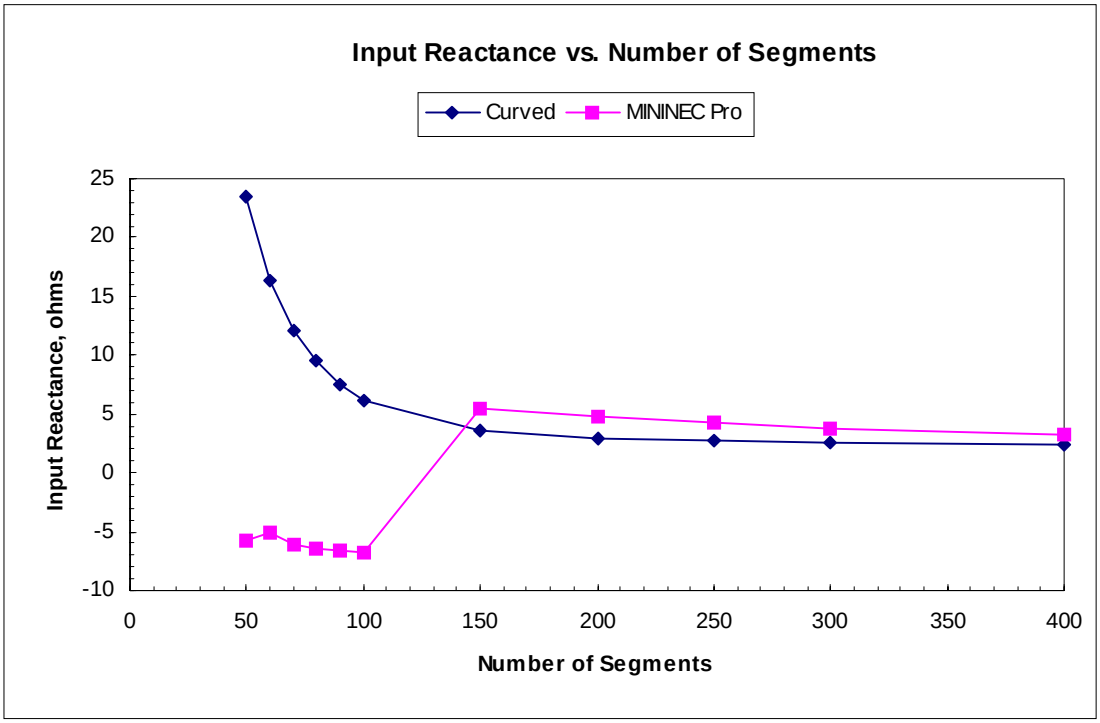

(b) Input reactance.

Figure 5.6 Axial mode helix over ground impedance convergence plots.
Helix parameters: $\rho = 0.159\lambda$, $\alpha = 13°$, $N = 10$, $a = 0.001\lambda$, $z_o = 0.1\lambda$, $Feed = 0.05\lambda$

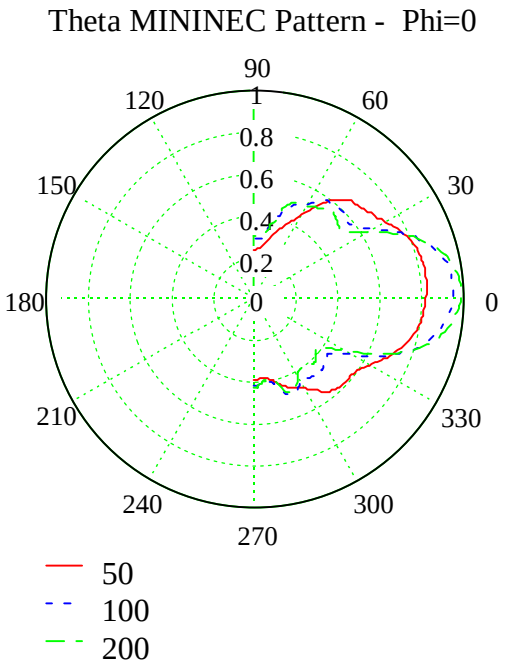

(a) MININEC patterns.

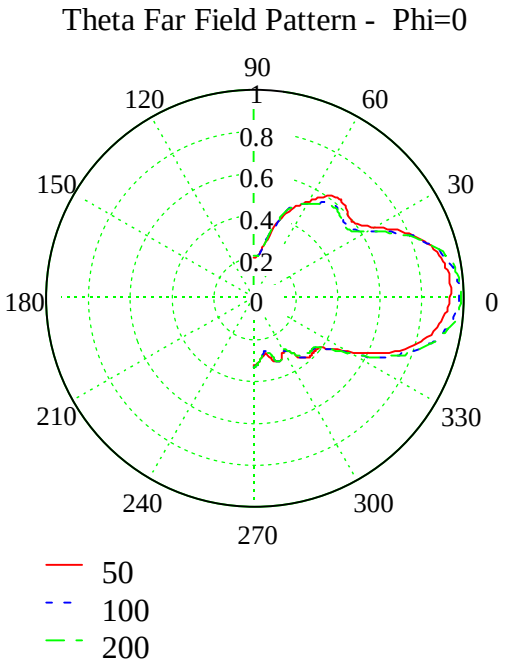

(b) Curved code patterns.

Figure 5.7 Theta-component of far-field electric field patterns for axial mode helix over ground.
Helix parameters: $\rho = 0.159\lambda$, $\alpha = 13°$, $N = 10$, $a = 0.001\lambda$, $z_o = 0.1\lambda$, $Feed = 0.05\lambda$

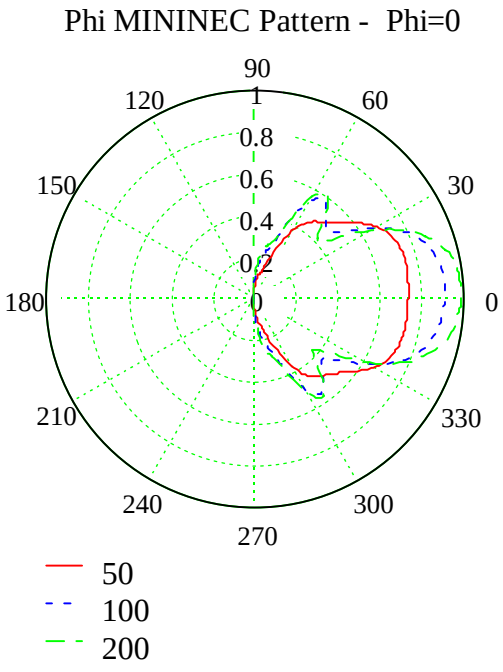

(a) MININEC patterns.

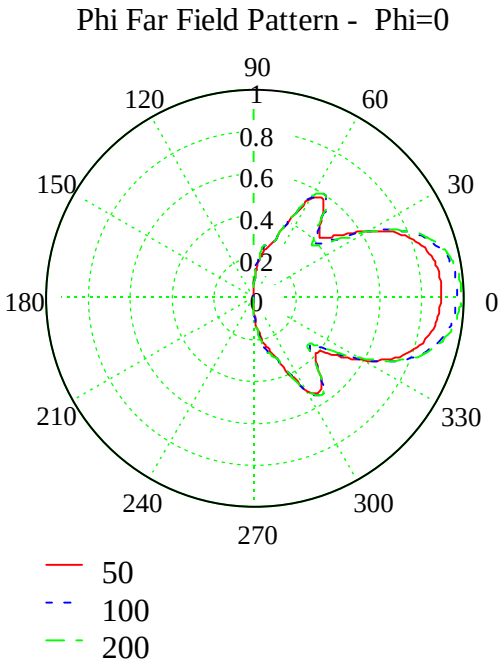

(b) Curved code patterns.

Figure 5.8 Phi-component of far-field electric field patterns for axial mode helix over ground.
Helix parameters: $\rho = 0.159\lambda$, $\alpha = 13°$, $N = 10$, $a = 0.001\lambda$, $z_o = 0.1\lambda$, $Feed = 0.05\lambda$

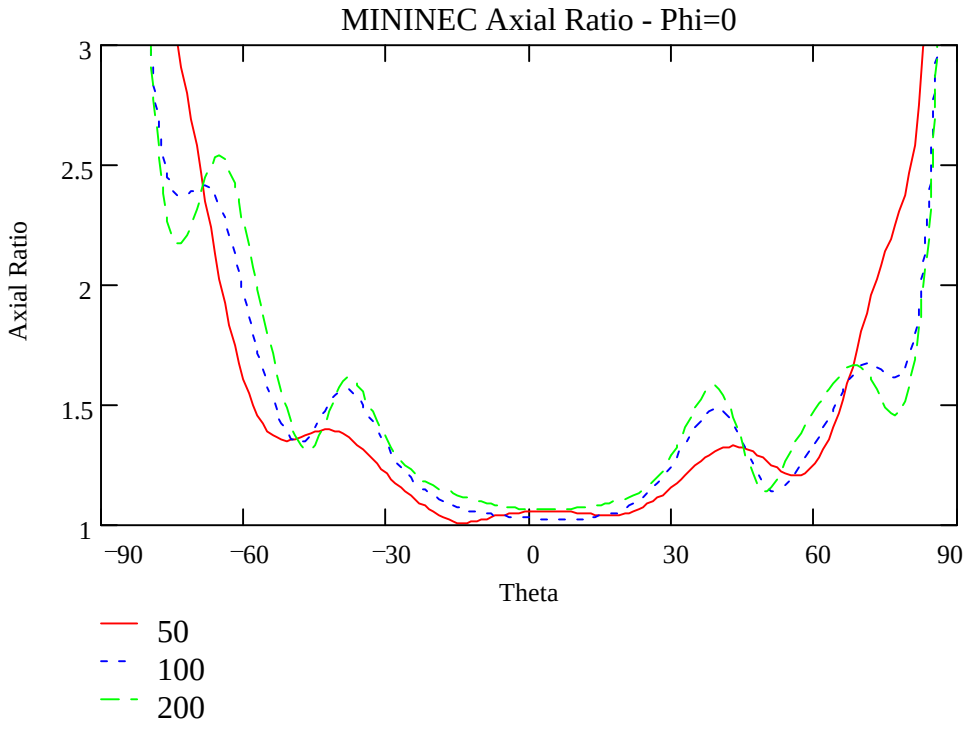

(a) Axial ratio from MININEC.

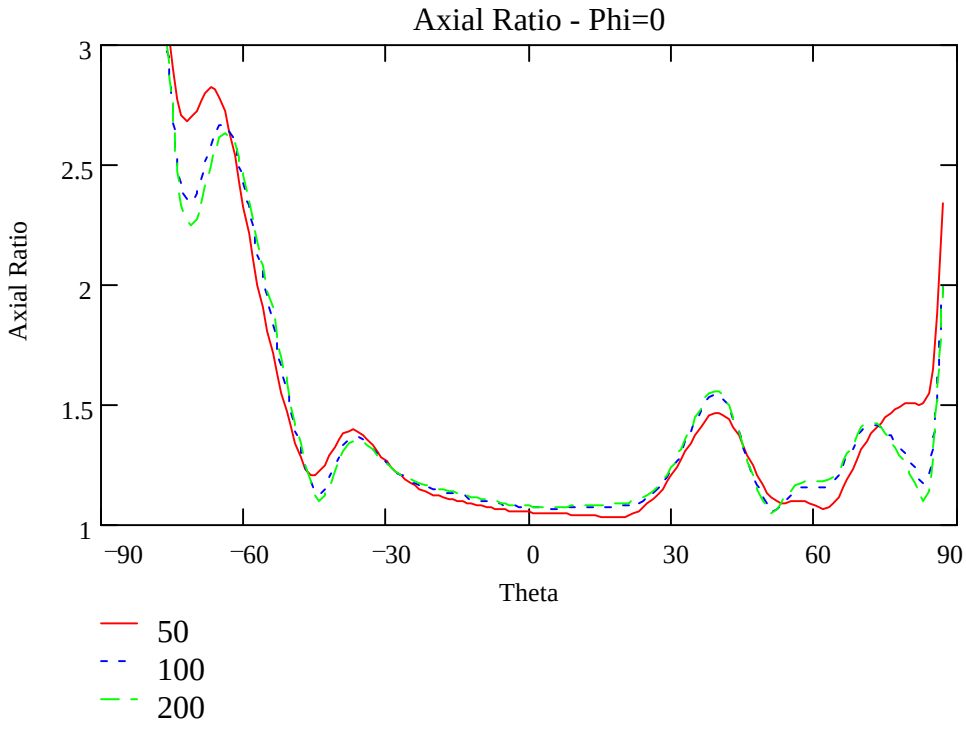

(b) Axial ratio from Curved code.

Figure 5.9 Axial ratio for axial mode helix over ground.
Helix parameters: $\rho = 0.159\lambda$, $\alpha = 13°$, $N = 10$, $a = 0.001\lambda$, $z_o = 0.1\lambda$, $Feed = 0.05\lambda$

than MININEC, particularly for the 50 segment case, but even the 100 and 200 segment examples show slightly lower local maximums at about $\theta = \pm 40°$ for the Curved code.

5.3 Bandwidth and Feed Effects of Axial Mode Helix Over Ground

As stated earlier in this chapter, an axial mode helix should operate over a frequency range such that its circumference is bounded by $\frac{3}{4}\lambda < C < \frac{4}{3}\lambda$. This corresponds to a bandwidth of approximately 1.78:1 or 56%. Fig. 5.10 shows the input impedance versus wavelength for two different feed structures computed using only the Curved code with a helix of 200 segments. The first feed structure is the single straight feed wire as shown in Fig. 5.5, and the second structure consists of two straight feed wires as shown in Fig. 3.1. Fig. 5.10 shows that the impedance behaves well for wavelengths from $0.8 < \lambda < 1.35$ meters. Compared to theory, the antenna falls a bit short of meeting the high frequency prediction of λ=0.75 m.

The bandwidth can be further validated by checking the antenna patterns at the band edges for the single feed wire. The patterns for wavelengths of 0.75 m, 0.8 m, and 1.35 m are shown in Figs. 5.11, 5.12, and 5.13, respectively. Fig. 5.11 shows that a wavelength of 0.75 m is definitely outside the range for good antenna pattern performance, but Fig. 5.12 and Fig. 5.13 show well formed patterns which supports the bandwidth predicted from the impedance plots of Fig. 5.10. Of course, other parameters such as gain and beamwidth could also be computed over the frequency range, but are not considered in this thesis.

There are two feed effects that will be considered further. The first is the effect of the feed location on the antenna input impedance. The geometry is shown in Fig. 5.14. For the 2 feed wire structure, the horizontal feed wire has 6 segments, and both feed structures have 8 segments on the vertical wire, which gives 9 feed locations indicated by the small hash marks. The helix parameters are those of Fig. 5.5 with a helix of 200 segments. Fig. 5.15 shows the input impedance versus the feed location on the vertical feed wire for the 1 and 2 feed wire structures. The input resistance for the 1 wire feed increases almost linearly as the feed location moves away from the ground plane, but the input resistance for the 2 wire feed is roughly constant as the feed location is varied. The general trend of the imaginary part of the input impedance is the same for both feed structures, but the 1 wire feed is resonant for a feed location between unknown 2 and 3 (about 0.02λ above ground) and the 2 wire feed is resonant for a feed location at unknown 5 (about 0.05λ above ground).

The effect of feed height, or the parameter z_o, on the input impedance is the second characteristic to be considered. The height of the vertical feed wire for both feed structures is increased in steps of 0.025λ, which is also the length of one segment. The voltage source is always located at the connection with the ground plane. Once again, the helix is described in Fig. 5.5 with 200 segments, and the horizontal wire of the 2 wire

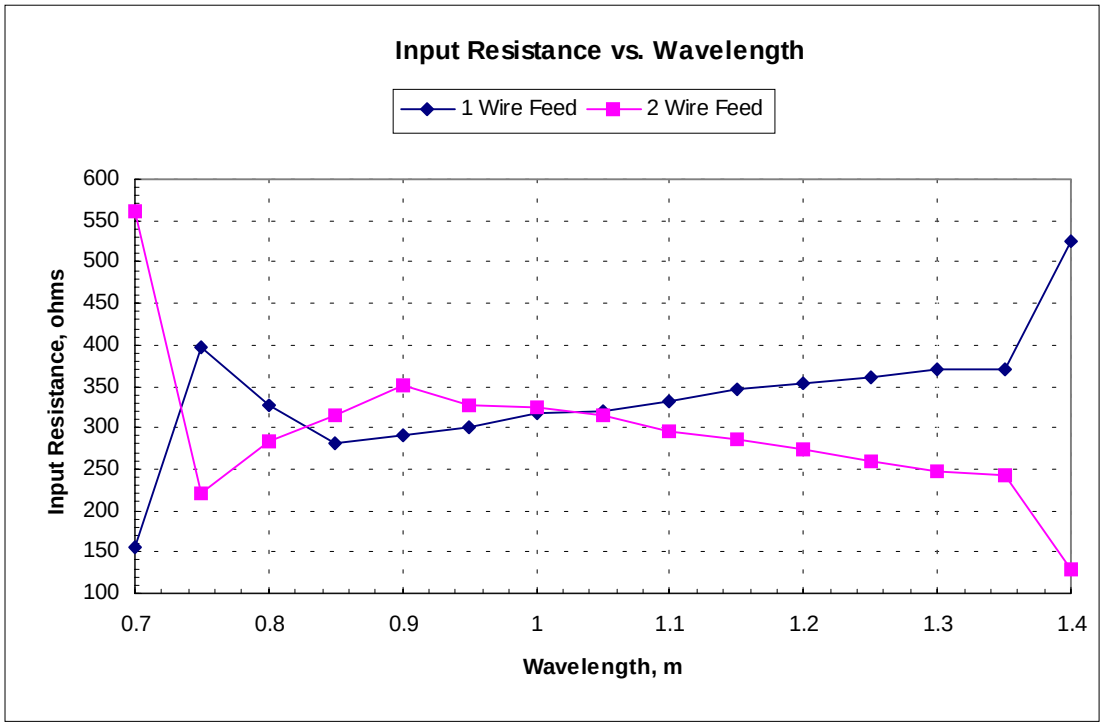

(a) Input resistance.

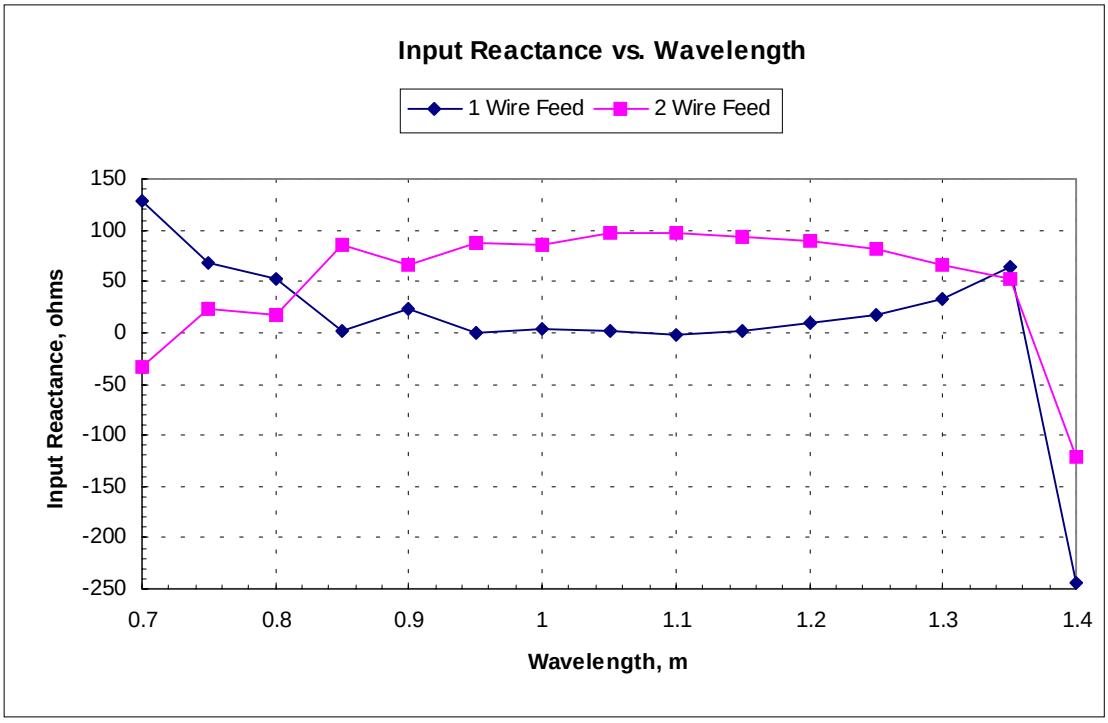

(b) Input reactance.

Figure 5.10 Input impedance vs. wavelength for axial mode helix over ground. Helix parameters: $\rho = 0.159\lambda$, $\alpha = 13°$, $N = 10$, $a = 0.001\lambda$, $z_o = 0.1\lambda$, $Feed = 0.05\lambda$

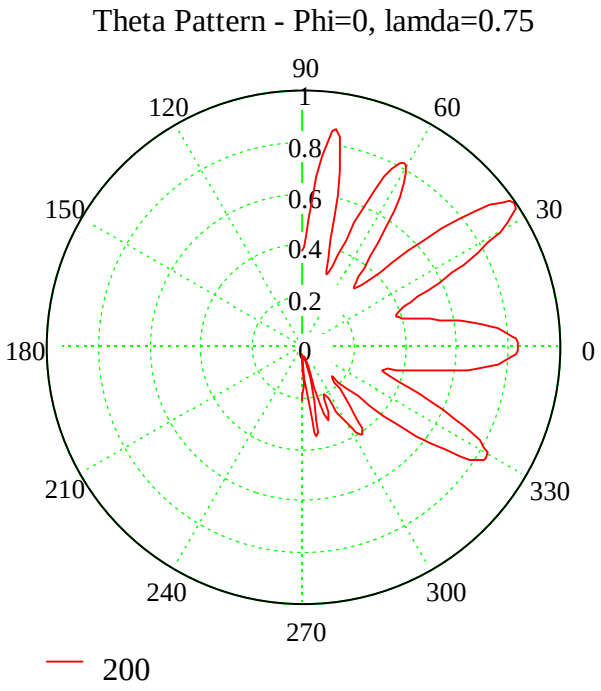

(a) Theta-component.

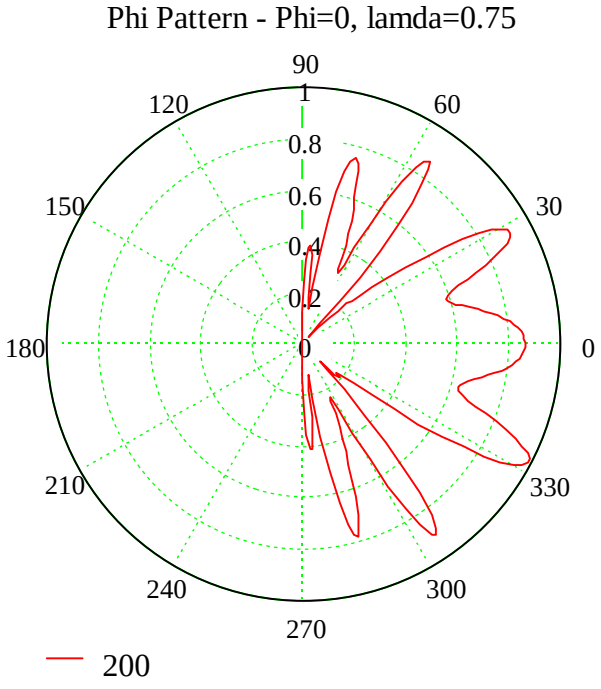

(b) Phi-component.

Figure 5.11 Far-field electric field patterns for axial mode helix over ground at $\lambda = 0.75$ m.
Helix parameters: $\rho = 0.159\lambda$, $\alpha = 13°$, $N = 10$, $a = 0.001\lambda$, $z_o = 0.1\lambda$, $Feed = 0.05\lambda$

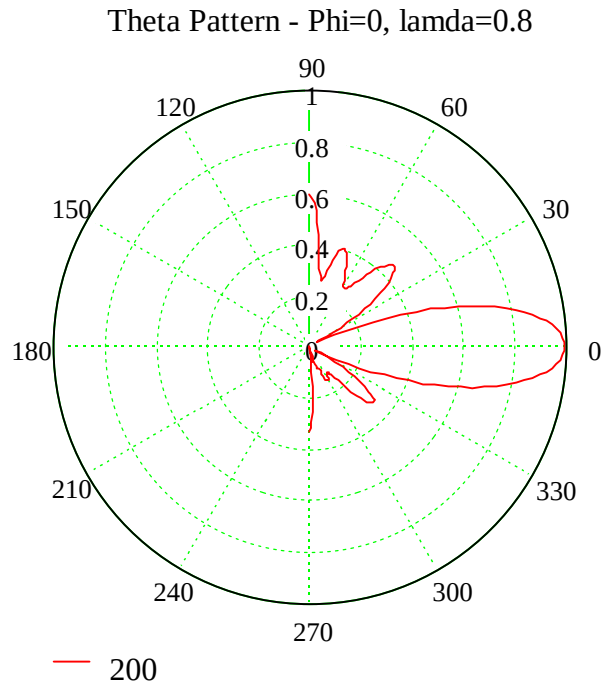

(a) Theta-component.

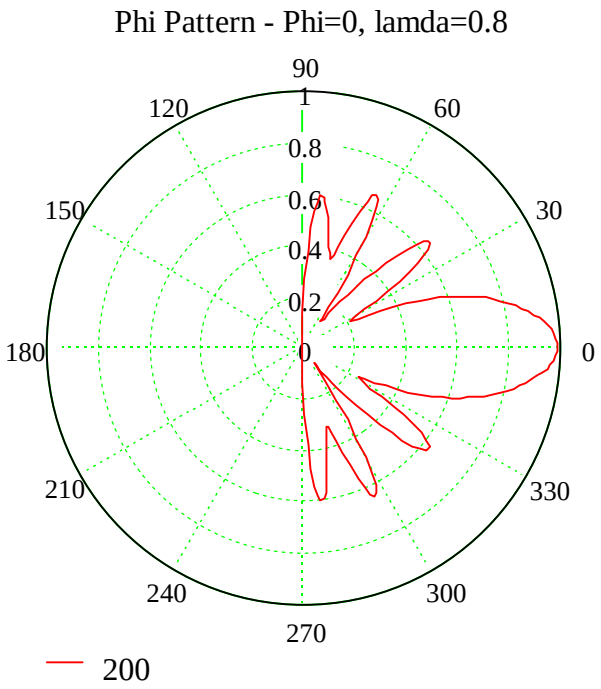

(b) Phi-component.

Figure 5.12 Far-field electric field patterns for axial mode helix over ground at $\lambda = 0.8$ m.
Helix parameters: $\rho = 0.159\lambda$, $\alpha = 13°$, $N = 10$, $a = 0.001\lambda$, $z_o = 0.1\lambda$, $Feed = 0.05\lambda$

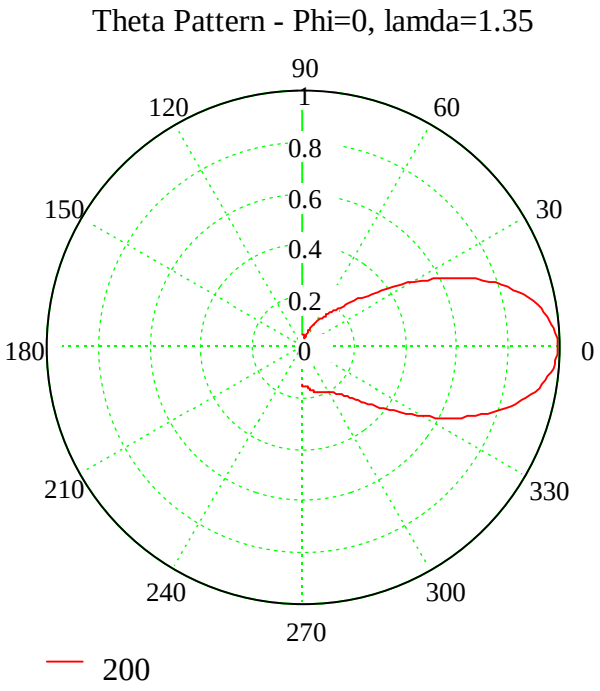

(a) Theta-component.

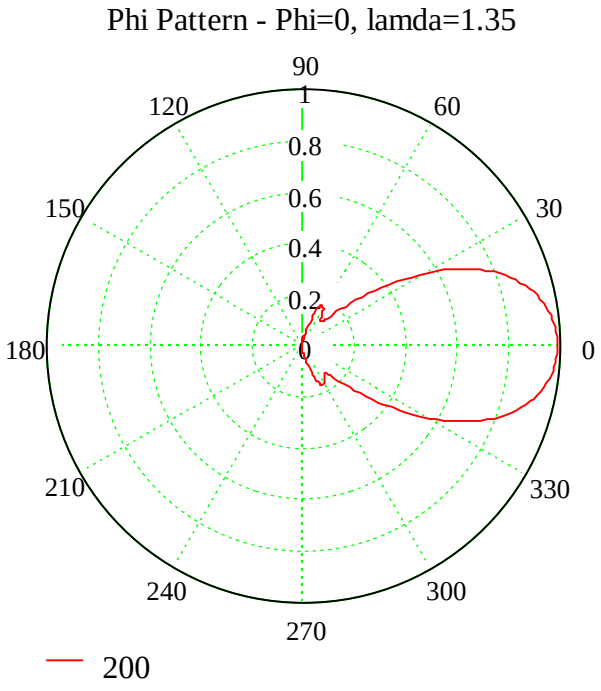

(b) Phi-component.

Figure 5.13 Far-field electric field patterns for axial mode helix over ground at $\lambda = 1.35$ m.
Helix parameters: $\rho = 0.159\lambda$, $\alpha = 13°$, $N = 10$, $a = 0.001\lambda$, $z_o = 0.1\lambda$, $Feed = 0.05\lambda$

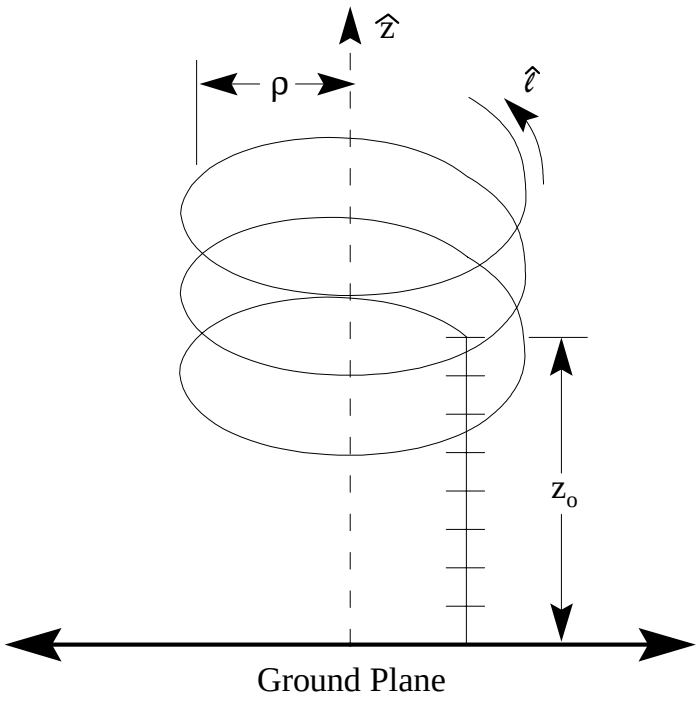

(a) 1 wire feed geometry.

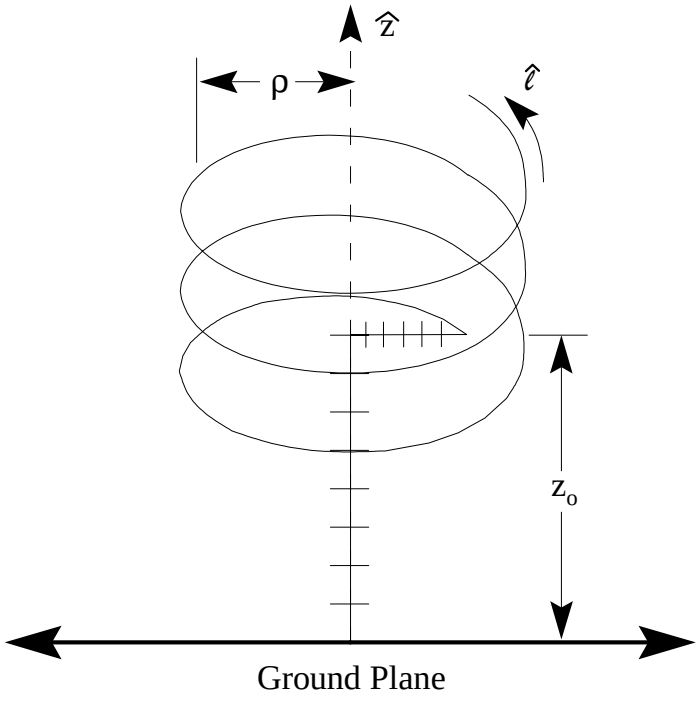

(b) 2 wire feed geometry.

Figure 5.14 Feed structure geometry for different feed locations.

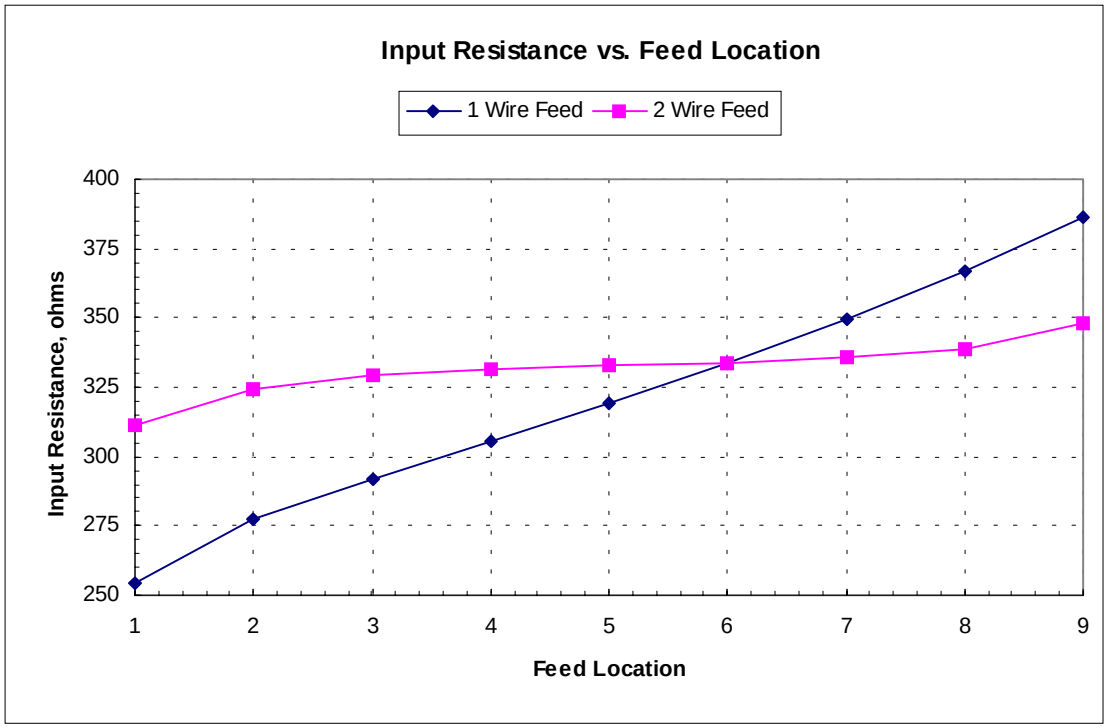

(a) Input resistance.

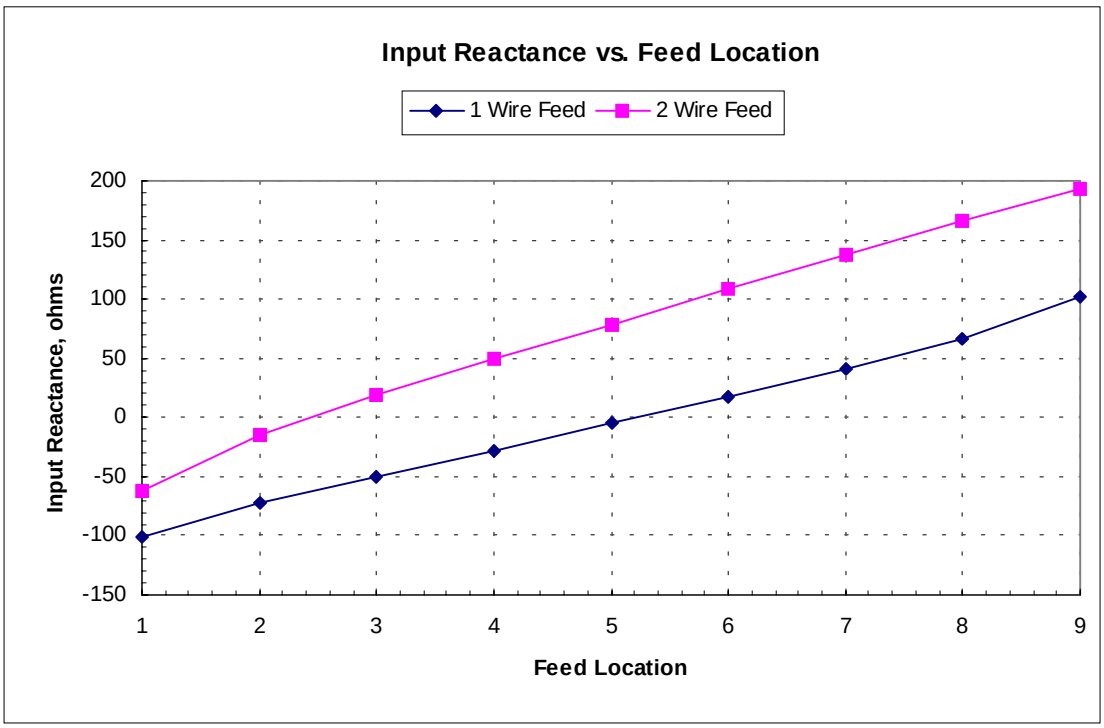

(b) Input reactance.

Figure 5.15 Input impedance vs. feed location for axial mode helix over ground. Helix parameters: $\rho = 0.159\lambda$, $\alpha = 13°$, $N = 10$, $a = 0.001\lambda$, $z_o = 0.1\lambda$, $Feed = 0.05\lambda$

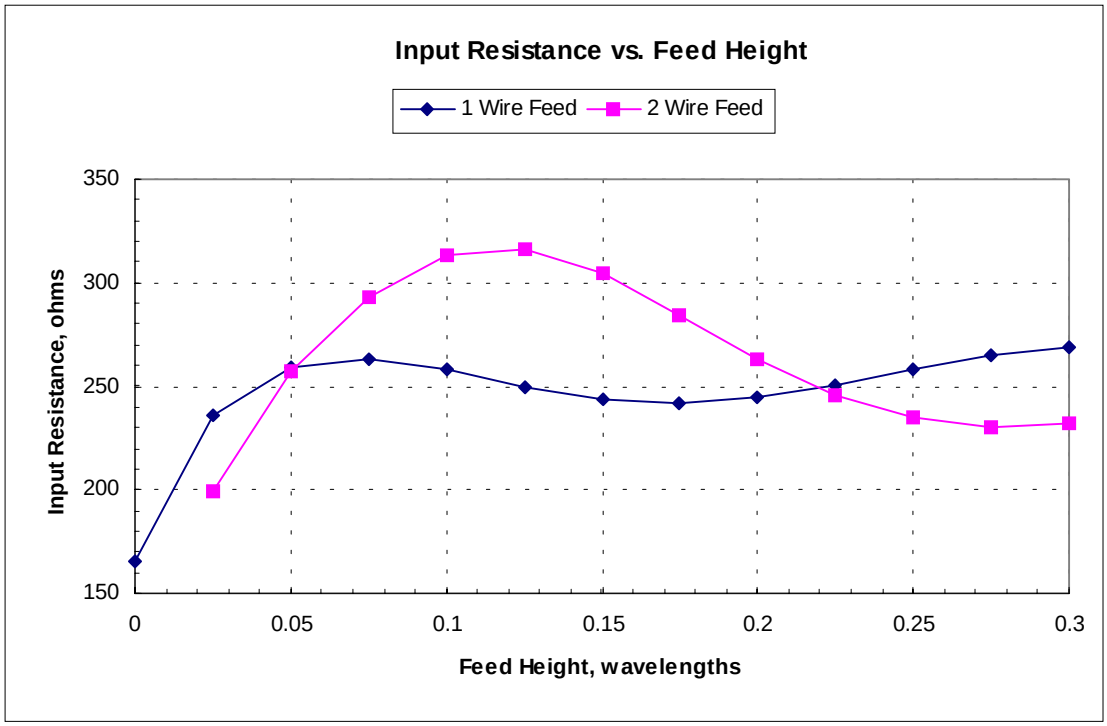

(a) Input resistance.

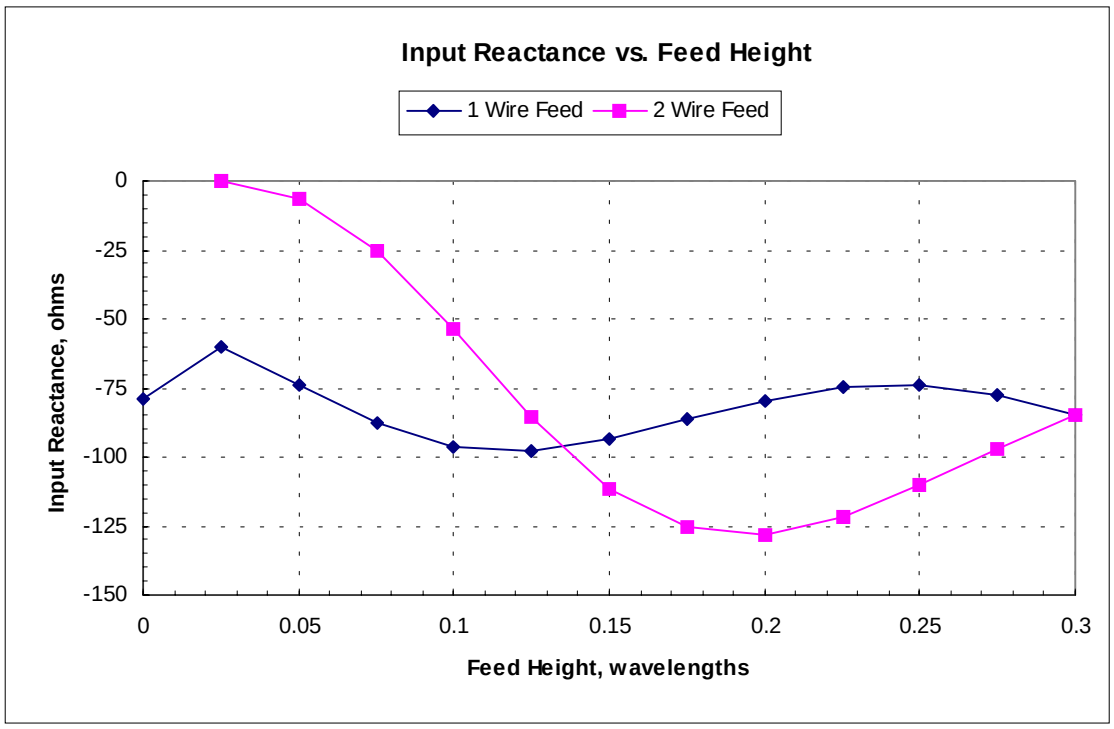

(b) Input reactance.

Figure 5.16 Input impedance vs. feed height for axial mode helix over ground. Helix parameters: $\rho = 0.159\lambda$, $\alpha = 13°$, $N = 10$, $a = 0.001\lambda$, $z_o = 0.1\lambda$, fed at ground

feed has 6 segments. Fig. 5.16 shows the input impedance of the antenna as the height of the helix off the ground plane is increased. The data for the 2 wire feed starts at a height of 0.025λ because a zero height does not make sense for this feed structure. Both the real and imaginary parts of the input impedance oscillate as the height increases, but the amplitude of the oscillations is greater for the 2 wire feed structure. Also, as the height increases the oscillations seem to be damping out. Only the 2 wire feed is resonant, which is for a height of 0.025λ. This gives a very short feed structure when compared to the helix radius of $\rho = 0.159\lambda$.

Another important consideration is comparison to measured data. Kraus (1950) performed many input impedance measurements for axial mode helices and found the input impedance to be nearly real with values from 100 to 200 ohms. In particular, Kraus gives the empirical formula $R = 140\dfrac{C}{\lambda}$ ohms $\pm 20\%$ for the input impedance of an axial mode helix for $12° < \alpha < 15°$, $\dfrac{3}{4}\lambda < C < \dfrac{4}{3}\lambda$, $N > 3$ turns, and fed at the ground plane. Kraus measured an axial mode helix with a single feed wire diagonally from the bottom end of the helix to the ground plane. The pitch of the diagonal feed wire was the same as the helix pitch angle. Using the Curved code to model a 10 turn axial mode helix with $\alpha = 13°$ and $C = \lambda$, the input impedance is $163.97 - j64.0\Omega$. The real part predicted by the Curved code is within the range of the values prescribed by the empirical relation. The slightly large imaginary part is probably due to feed modeling considerations, however the Curved code and MININEC both predict approximately the same input impedance.

5.4 Conclusions

The axial mode helix in free space was presented for comparison with the normal mode helix in the last chapter. Since approximating the current on the axial mode helix is more important than approximating the curve of the helix, the Curved code does not show as big an improvement over NEC and MININEC as for the normal mode helix. Despite this fact, anywhere from 2 to 4 times fewer unknowns can still be achieved with the Curved code. When the axial mode helix is placed over a ground plane with a straight feed wire no improvement in input impedance convergence is found. This is because the voltage source is located on the straight feed wire where both the Curved code and MININEC perform about equally. However, the Curved code does show an improvement in pattern convergence for the axial mode helix over ground. Bandwidth, feed location, and feed height were also investigated. The axial mode helix over ground was found to operate well for a turn circumference bounded by $0.8\lambda < C < 1.35\lambda$. The effects of feed location and feed height on input impedance were shown for 1 and 2 feed wire structures. The axial mode helix example was resonant when the source was located in the center of the 1 wire feed example, which was about double the height above ground required to resonate the 2 wire feed example. The input impedance to the axial mode helix oscillates as the height of the helix above the ground plane increases, but the effect of the 2 different feed structures becomes less significant as the height increases.

6. Conclusions

A more efficient method for the analysis of curved wire antennas has been presented in this thesis. By using curved basis and testing functions which exactly follow the contour of the antenna, fewer unknowns can be used compared to programs such as MININEC and NEC, which use a straight wire approximation. The helix antenna has been used as an example to demonstrate the improvement found when using the Curved code. As a secondary goal of this thesis, the Curved code is used to analyze some interesting properties of the helix, such as bandwidth and feed effects.

The background theory for wire antenna analysis using the Method of Moments was presented in Chapter 2. This includes the derivation of the electric field integral equation for general structures and the basics of the Method of Moments, which were then applied to a straight wire antenna. The thin wire approximation and delta gap source model were also described. As an example, a resonant center fed dipole was analyzed using the Method of Moments with piece-wise sinusoidal basis functions and pulse testing functions.

In Chapter 3, the electric field integral equation for straight wires was extended for use with arbitrary wire antenna structures. The helix geometry and terminology was presented as the primary example of this thesis. The general electric field integral equation presented in this chapter can be applied to any wire antenna by defining the appropriate unit vector, $\hat{\ell}$, and position vector, $\bar{r}$. Triangular basis functions and pulse weighting functions are used in the analysis of the helix antenna. The formulation for wire connections and a pec ground plane are also presented.

Using the theory for the Curved code, a normal mode helix is analyzed in Chapter 4. First, a normal mode helix with a pitch angle of $\alpha = 89°$ is discussed for code validation purposes. The large pitch angle allows the helix to approximate a straight wire for comparison to the results of Chapter 2. Both a half-wave dipole in free space and a monopole connected to an infinite pec ground gave excellent agreement. A method of modeling a normal mode helix with an inductively loaded dipole was also presented. This technique is limited by the ability of the theory to determine a priori the required load, but the theory should predict the required inductive load more accurately for more tightly wound helices. A normal mode helix has a turn radius much smaller than a wavelength, resulting in a current distribution which is approximately uniform for one turn. Since the current is nearly uniform, accurately modeling the curve of the helix is of primary importance. This is the strength of the Curved code. Compared to MININEC and NEC an improvement of about 8:1 is achieved. In other terms, the Curved code gives accurate results for approximately 5 segments per turn versus 40 segments per turn for the other codes.

The axial mode helix, presented in Chapter 5, has a turn length of approximately one wavelength and is usually backed by a ground plane. An axial mode helix in free space was first analyzed for comparison with the normal mode helix in Chapter 4. An

improvement of between 2 and 4 times fewer unknowns is found when using the Curved code as compared to 8 times fewer unknowns for the normal mode helix. The difference in the improvement between to the two helix antennas is due to their current distributions within a single turn. Since current on an axial mode helix varies for approximately a full wavelength around one turn, it is more important to accurately model the current than to model the curve of the helix. The strength of the Curved code is of secondary importance and a smaller impedance improvement results. The axial mode helix over ground shows no significant improvement in impedance convergence because the voltage source is located on the straight feed wire. However, an improvement in radiation pattern convergence is found. The Curved code was also used to analyze the bandwidth and some feed effects for the axial mode helix over ground. A 1 and 2 wire feed example are used to examine the effects of voltage source location and helix height off ground plane. It was found that a source located in the center of the 1 wire feed example and about half that height above ground for the 2 wire feed example give resonant behavior. The input impedance oscillates as the height of the helix above ground increases, however the differing effects on the input impedance for the 1 and 2 wire feed examples become less significant as the height of the helix above ground increases.

6.1 Recommendation for Future Work

Potential for future work exists in the area of enhancements to the Curved code. Tapered helices, spirals, arbitrary helix orientations, and finite ground could all be added to the code. In addition to these improvements the Curved code's integral routines could be improved through the use of more sophisticated algorithms or through the use of semi-analytic techniques which would lower the required computation time. The use of the full kernel, instead of the thin wire approximation, would also improve the accuracy of the Curved code. The curved techniques may be applied to more complicated structures, possibly including curved surfaces.

References

Balanis, C. A. (1989), *Advanced Engineering Electromagnetics*, John Wiley & Sons, New York.

Burke, G. J. (1992), *NEC4, Part II: Program Description - Theory*, January.

Champagne, N. J., Williams, J. T., and Wilton, D. R. (1992), "The use of curved segments for numerically modeling thin wire antennas and scatters," *IEEE Trans. Antennas Propagat.*, vol. 40, pp. 682-689, June.

Davis, W. A. (1995), "Numerical methods for wire structures," draft. (http://www.vt.edu:10021/eng/ee/faculty/Wdavis/antenna/)

Desplanches, B., Sharaiha, A., and Terret, C. (1997), "Numerical analysis of helical antennas backed by finite ground planes," *Microwave and Optical Technology Letters*, vol. 15, pp.352-355, August 20.

Edminister, J. A. (1993), "Theory and problems of elecromagnetics 2/ed," *Schaum's Outline Series*, McGraw-Hill, New York.

Haapala, P., Vainkainen, P., and Eratuuli, P. (1996), "Dual frequency helical antennas for handsets," *IEEE Veh. Tech. Conf.*, vol. 1, pp. 336-338.

Hallen, E. (1938), "Theoretical investigations into the transmitting and receiving qualities of antennae," *Nova Acta Regiae Soc. Sci. Upsaliensis*, Ser. IV, pp. 1-44.

Harrington, R. F. (1968), *Field Computation by Moment Methods*, Macmillan, New York.

Hui, H. T., Yung, E. K. N., Leung, K. W. (1997), "Numerical and experimental studies of a helical antenna loaded by a dielectric resonator," *Radio Science*, vol. 32, pp. 295-304, March-April.

Jensen, M. A. and Rahmet-Samii, Y. (1994), "Electromagnetic characteristics of superquadratic wire loop antennas," *IEEE Trans. Antennas Propagat.*, vol. 42, pp.264-269, February.

Khamas, S. K. and Cook, G. G. (1997), "Moment-method analysis of printed wire spirals using curved piecewise sinusoidal subdomain basis and testing functions," *IEEE Trans. Antennas Propagat.*, vol. 45, pp.1016-1022, June.

Khamas, S. K, Cook, G.G., Waldron, R. J., and Edwards, R. M. (1997), "Moment method analysis of printed single-arm wire spiral antennas using curved segments," *IEE Proceedings-Microwaves Antennas and Propagation*, vol. 144, pp. 261-265, August.

King, R. W. P. (1967), "The linear antenna - eightly years of progress," *Proc. IEEE 55*, pp. 2-16.

Kraus, J. D. (1950), *Antennas*, McGraw-Hill, New York.

Li, R. L., Ni, G. Z., Yu, J. H., and Jiang, Z. J. (1996), "A new numerical technique for calculating current distribution on curved wire antennas - parametric B-spline finite element method," *IEEE Trans. Magnetics*, vol. 32, pp. 906-909, May.

Marsh, J. A. (1951), "Measured current distribution on helical antennas," *Proc. I.R.E.*, vol. 39, pp. 668-675, June.

Meggyesi-Mitschang, L. N. and Putnam, J. M. (1985), "Electromagnetic scattering from extended wires and two- and three-dimensional surfaces," *IEEE Trans. Antennas Propagat.*, vol. 33, pp. 1090-1100, October.

Mei, K. K. (1965), "On the integral equations of thin wire antennas," *IEEE Trans. Antennas Propagat.*, vol. 13, pp.374-378, May.

Miller, E. K., and Deadrick, F. J. (1975), "Some computational aspects of thin-wire modeling," Chapter 4 in *Numerical and Asymptotic Techniques in Electromagnetics*, R. Mittra editor, Springer-Verlag, New York.

Pocklington, H. C. (1897), "Electrical oscillations in wire," *Camb. Phil. Soc. Proc. 9*, 324-332.

Poggio, A. J. and Miller, E. K. (1987), "Integral equation solutions of three-dimensional scattering problems," Chapter 4 in *Computer Techniques for Electromagnetics*, R. Mittra editor, Hemisphere Publishing Corporation, Washington.

Richmond, J. H. (1965), "Digital solutions of the rigorous equations for scattering problems," *Proc. IEEE 53*, pp. 796-804.

Rockway, J. W. and Logan, J. C. (1995), *MININEC Professional for Windows*, EM Scientific, Inc.

Rogers, S. D. and Butler, C. M. (1997), "Reduced Rank Matrices for Curved Wire Structures," *IEEE-Antennas-and-Propagation-Society,-AP-S-International-Symposium-(Digest). v 1 1997*, IEEE, Piscataway, NJ, USA,97CB36122. pp. 68-71.

Roy, M. N. (1969), "Investigation of normal mode helices," *Int. J. Electronics*, vol. 26, pp. 573-578.

Stutzman, W. L. (1993), *Polarization in Electromagnetic Systems*, Artech House, Inc., Boston.

Stutzman, W. L. and Thiele, G. A. (1998), *Antenna Theory and Design*, 2nd edition, John Wiley & Sons, New York.

Wheeler, H. A. (1947), "A helical antenna for circular polarization," *Proc. I.R.E.*, vol. 35, pp. 1484-1488, December.

Wilton, D. R. and Butler, C. M. (1976), "Efficient numerical techniques for solving Pocklinton's equation and their relationship to other methods," *IEEE Trans. Antennas Propagat.*, vol. 24, pp. 83-86, January.

Vita

Eric David Caswell was born in Ravena, New York on May 6, 1973. His family moved to Calabash, North Caroline in June 1996 and he now considers this his home town. He received a B.S.E.E. in May 1995 and a M.S.E.E. in December 1998 both from Virginia Tech. He is currently pursuing a Ph.D. in electrical engineering at Virginia Tech.